Master Thesis

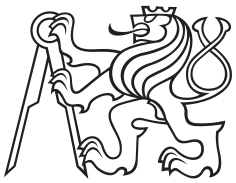

Czech Technical University in Prague

F3

Faculty of Electrical Engineering
Department of Measurement

Contacless measurement of electric currents

Bc. Andrey Chirtsov

Supervisor: Prof. Ing. Pavel Ripka, CSc.
Field of study: Cybernetics and Robotics
May 2019

MASTER'S THESIS ASSIGNMENT

I. Personal and study details

Student's name: **Chirtsov Andrey** Personal ID number: **434768**

Faculty / Institute: **Faculty of Electrical Engineering**

Department / Institute: **Department of Measurement**

Study program: **Cybernetics and Robotics**

Branch of study: **Cybernetics and Robotics**

II. Master's thesis details

Master's thesis title in English:

Contacless Measurement of Electric Currents

Master's thesis title in Czech:

Bezkontaktní měření elektrických proudů

Guidelines:

1) Design a three-phase busbar transducer for large currents with zero crosstalk between phases and minimized influence of external electrical currents and magnetic fields and calibrate it.
2) Descibe the construction of rectangular current transducer and compare its pararameters with commercially available transducer LEM.
3) Characterize the parameters of all three mentioned sensors in wide temperature range and compare their parameters with values in literature.

Bibliography / sources:

[1] Ripka, P., Chirtsov, A.: Busbar current transducer with suppression of external fields and gradient;, IEEE Transactions on Magnetics Vol. 54 Issue: 11, 2018, Article # 4002504
[2] Ripka, P., Grim, V., Petrucha, V.: A busbar current sensor with frequency compensation:
IEEE Trans. Magn. Vol. 53 (2017), Issue 4, paper # 4000505
[3] Ripka, P., Chirtsov, A.: Influence of External Current on Yokeless Electric Current Transducers, IEEE Transactions on Magnetics, 2017, Volume: 53, Issue: 11, paper # 4003904 ,

Name and workplace of master's thesis supervisor:

prof. Ing. Pavel Ripka, CSc., Department of Measurement, FEE

Name and workplace of second master's thesis supervisor or consultant:

Date of master's thesis assignment: **31.01.2019** Deadline for master's thesis submission: **24.05.2019**

Assignment valid until:
by the end of summer semester 2019/2020

prof. Ing. Pavel Ripka, CSc. Supervisor's signature	Head of department's signature	prof. Ing. Pavel Ripka, CSc. Dean's signature

III. Assignment receipt

The student acknowledges that the master's thesis is an individual work. The student must produce his thesis without the assistance of others, with the exception of provided consultations. Within the master's thesis, the author must state the names of consultants and include a list of references.

.	
Date of assignment receipt	Student's signature

Acknowledgements

I would like to express my deep gratitude to Professor Pavel Ripka, my research supervisor, for his patient guidance, enthusiastic encouragement and useful critiques of this research work.

I would also like to thank Ing. Mehran Mirzaei for his advice and assistance in the analytical framework and Mr. Oldřich Jandl for his support in the measurements.

Finally, I wish to thank my parents for their support and encouragement throughout my study.

Declaration

I declare that the presented work was developed independently and that I have listed all sources of information used within it in accordance with the methodical instructions for observing the ethical principles in the preparation of university theses.

Prague, 24^{th} May 2019

Prohlašuji, že jsem předloženou práci vypracoval samostatně, a že jsem uvedl veškeré použité informační zdroje v souladu s Metodickým pokynem o dodržování etických principů při přípravě vysokoškolských závěrečných prací.

V Praze, 24. května 2019

Abstract

Three-phase busbar current transducer is designed in this thesis. Suppression of the external magnetic field and field gradients up to 2nd order is achieved by using of 6 microfluxgate sensors. The 3D FEM model and analytical solution is confirmed by the measurements. The suppression 15x of the external field is achieved. The analytical solution is presented with the deriving formulas.

Rectangular current transducer based on the 16 microfluxgate sensors is presented in the 2nd part of this thesis, the comparison of the industrial standard sensor LEM HOP-800SB and yokeless sensor is performed, namely, the temperature offset drift, noise and crosstalk error.

Keywords: DRV425, Busbar sensor, current sensors, integrated fluxgate, microfluxgate, magnetic sensor

Supervisor: Prof. Ing. Pavel Ripka, CSc.
A4-104a,
Technická 2,
16027 Praha 6

Abstrakt

V této diplomové práci je navržen třífázový proudový snímač. Potlačení vnějšího magnetického pole a gradientů pole až do 2. řádu je dosaženo použitím 6 senzorů microfluxgate. 3D simulace metodou konečných prvků a analytické řešení je potvrzeno měřením. Dosahuje se potlačení 15x vnějšího magnetického pole. Analytické řešení je prezentováno pomocí odvozených vzorců.

V druhé části této práce je uveden obdélníkový proudový snímač založený na 16 mikrofluxgate senzorech, u kterého je provedeno srovnání s průmyslovým standardem LEM HOP-800SB, a to teplotní drift, šum a přeslechová chyba.

Klíčová slova: DRV425, Senzor proudu, fluxgate senzor, magnetický senzor

Překlad názvu: Bezkontaktní měření elektrických proudů

Contents

Figures

Tables

Chapter 1

Introduction

Firstly, the current was described and quantified by French physicist and mathematician André-Marie Ampère in the late 18^{th} century, as the flow of electricity along a conductor. Ampère's rule was formulated to determine the effect of a magnetic field on a magnetic needle. According to this conclusion, the north pole will be at the end of the rod to the left of a person who moves in the direction of the current and is facing it. Soon, the author confirmed the interaction between the electric currents, called Ampère's law. It shows the strength of the magnetic field in relation to the conductor inside it. The Ampère empirically proved that the parallel conductors begin to attract each other as the current moves in one direction and repel as it passes in the opposite direction. This experiment formed the basis for the later development of all the in-circuit current measurement instruments of moving-coil types. Later, the Ampère has developed the first measuring current system and called his device "galvanometer" because electrical currents were then called galvanic. It is worth noting that the first measurement system for the current was non-contact. The well-known Ohm's law was discovered after Ampère's discovery. Even nowadays we can see continuous improvement and developmental abundance of technology for measuring current.

Measurement of the voltage in the electronic system does not need the invasion and can be easily done at any point of the system without affecting the system performance. On the other hand, the current measurement does need the invasion as it requires insertion of the sensor which introduces a risk of affecting system performance or can cause the circuit degradation. The electric current is an essential parameter that needs to be monitored in most systems including power and instrumental. Different types of the current sensors will be described below.

1.1 Current sensors

1.1.1 Current shunts

The current shunt is probably the most common and simplest device for the current measurement. The measuring shunt is a four-clamps precision resistor. Two input terminals, with which current is supplied and two output clamps

for measurement of the voltage drop across the shunt. Ohm's law (1.1) is applied to convert the measured voltage to the current.

$$I = \frac{U}{R} \tag{1.1}$$

Where I is the unknown current, U is the measured voltage, and R is the shunt resistance.

Shunts are made from manganin. If the shunt is designed for a small current (up to 30 A), then it is usually embedded in the instrument case (internal shunts). Instruments with external shunts are used to measure high currents. In this case, the power dissipated in the shunt does not heat the instrument.

Shunt for 2000 A is shown in Figure 1.1. It has massive tips made of copper, which serve to remove heat from the manganin plates soldered between them. Clips of the shunt A and B are connected to the current. The voltmeter is connected to the potential terminals C and D, between which the resistance of the shunt is enclosed. Errors from contact resistances are eliminated with the 4-terminals connection. Shunts are divided into accuracy classes 0.02; 0.05; 0.1; 0.2 and 0.5. The number that determines the accuracy class indicates the tolerance of the shunt resistance as a percentage of its nominal value.

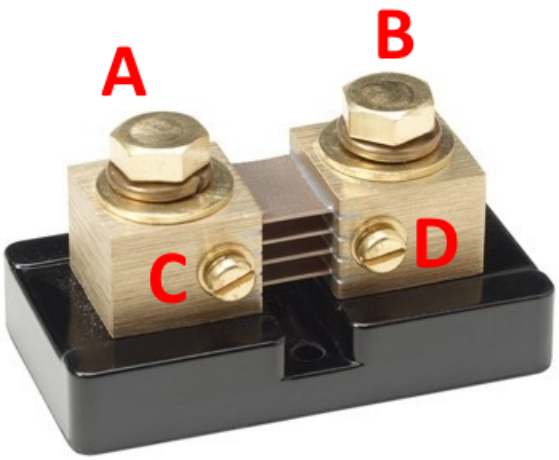

Figure 1.1: External Shunt 2000 $A/50\ mV$, accuracy class - 0.5 [1]

- Advantages
  - Simple device with no moving parts
  - High measurement accuracy, reliability
  - Low cost
  - AC and DC current measurement

- Unaffected by the adjacent conductors
- Wide range of the temperature (necessary to consider the temperature coefficient of the resistor and to avoid its heating)

- Disadvantages
  - The output is not galvanically isolated from the sensed current.
  - Power loss due to power dissipation
  - Load to the measured circuit
  - System must be broken to insert the shunt
  - Sensing voltage in the low-millivolt (mV) range (thermoelectric voltage can affect the reading)
  - The carbon dust or metallic particles can affect the shunt accuracy (conductive dirt)

1.1.2 Current Transformers

The current transformer is designed to convert measured current to a value convenient for sensing. The primary winding of the current transformer is connected in series with the measured alternating current, and the measuring instruments are connected to the secondary one. These are used extensively in the power utility industry as the current step down transformers. The current flowing through the secondary winding of a current transformer is proportional to the current flowing in its primary winding.

Current transformers (CTs) are widely used for measuring electric current and in relay protection devices of electric power systems, in connection with which they are subject to high accuracy requirements. CTs provide measurement security by isolating measuring circuits from a high-voltage primary circuit, often hundreds of kilovolts (kV).

There are high requirements for accuracy for CTs. As a rule, CTs are made with two or more groups of secondary windings: one is used to connect protection devices, and the other, more accurate, to connect measuring devices (for example, electric meters).

The second division of the CTs is the single-turn primary, open-aperture type. Clamp-on current transformer is a measuring transducer with which you can measure a large current in a conductor without breaking the circuit. The principle of operation of the transducer is as follows: magnetic induction is created around the conductor through which the primary (high) current passes. The magnetic flux is concentrated in the (usually toroidal) magnetic core. Using this core improves suppression of the external fields and makes the sensor insensitive to the position of the measured conductor. The electromotive force (EMF) induced by a field in a wire with a primary current in another secondary conductor is proportional to the primary current. Measuring the voltage on a shunt connected to the secondary current circuit allows determining the value of the measured primary current.

Figure 1.2: a) Closed [2] and b) open-on clamps [3]

- Advantages
  - Portable
  - Galvanic isolation
  - No need for circuit interruption
  - Low cost because of the design simplicity
- Disadvantages
  - Only AC current
  - Generally calibrated for operation at one frequency (use other frequencies or different shape measured signal can cause inaccuracy)
  - Require magnetic core

1.1.3 DC current comparator

DC current comparators are precise devices which are based on the fluxgate effect. The core consists of two detection rings excited on the opposite directions by the excitation winding N_{exc}. The synchronous detector (PSD) is used to extract the second harmonic from the induced voltage in detection winging N. The output of the PSD is filtered and amplified, and controls the DC compensation current I_2. The output of DC comparator is derived from shunt resistor R (in the ideal case $N_1 I_1 = N_2 I_2$). The magnetic shielding which is shown in Figure 1.3 has two options: it reduces the leakage fluxes originating from the non-homogeneity of the detection cores and the non-homogeneity of the windings, and it also provides magnetic shielding against external fields [9]. The schematic of the DC comparator is shown in Figure 1.3.

- Advantages
  - Galvanic isolation
  - Wide range of the operating currents (up to 10000 A)

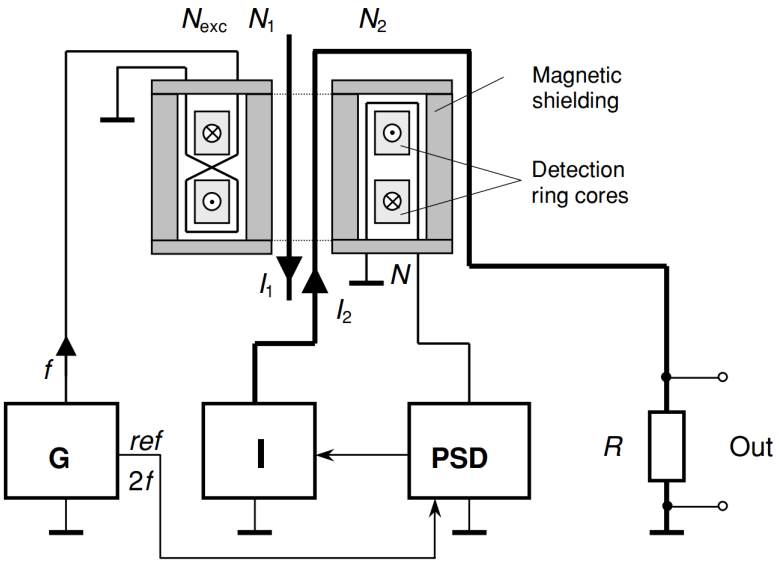

Figure 1.3: DC current comparator - schematic [4]

- High measurement accuracy
- Can operate in a hostile environment

- Disadvantages
  - Only DC and low-frequency current
  - High price
  - External AC source is required, transducer output is not galvanically isolated from this source

1.1.4 Hall effect probe

The Hall sensor is placed into a magnetic core with the placed inside a measured conductor in the open magnetic section. The principal scheme is shown in Figure 1.4. The compensated sensors also exist and brings more improvement. More information about the Hall sensor and their usage for the current sensor will be given in State-Of-The-Art section.

- Advantages
  - Simplicity
  - Low price
  - Galvanic isolation
  - AC and DC currents
  - Wide bandwidth
  - Contactless measurement

- Disadvantages

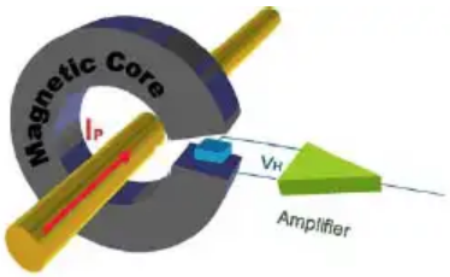

Figure 1.4: Illustration of the basic principle and structure of the Hall-Effect open loop current sensor. [5]

- Influenced by the external currents close to the airgap
- Large temperature dependence
- Significant noise

1.2 State-Of-The-Art

Hall sensors are usually inserted in the narrow airgap in the yoke, and since their sensitivity axis is perpendicular to the case, they are fit good for this role, and therefore dominate in this application. However, introducing the small gap into the magnetic yoke reduces the immunity to the external field because the magnetic flux created by the external currents can penetrate inside the magnetic material. [10]. Similar transducers have small fluxgate sensor in the slot of the yoke, or the whole yoke is AC excited and works as a fluxgate sensor. [11, 12]. There are also transducer configurations with the closed-loop and accuracy below 0.1% is achieved, but there is a need for the additional electronics, signal processing that greatly increases the price, power consumption, and size. Therefore, the open-loop configuration is often used for many applications. Sensitivity drift of Hall sensor can be compensated using the fully integrated microsystem to less than 80 ppm/°C, and nonlinearity below 0.08%. [13].

However, the large AC and DC currents are often measured without the magnetic yoke because for this application the magnetic yoke becomes too heavy and large, and there is the requirement to prevent the saturation of the magnetic material and ensure the safety distance from the measured conductor. Hall sensors, Anisotropic magnetoresistive sensors (AMR), and microfluxgate sensors are suitable for this application. Advantage of this solution is no threat of yoke saturation by the overcurrent [14]. Commercially available yokeless current sensor such as Senis BBM [15] use the Hall sensors on both sides of the busbar, range of the transducer varies from 100 to 3000 A. This configuration enables effectively cancel only the homogeneous part of the external magnetic fields without magnetic cores, but on the other hand, this sensor has the linearity error up to 1.5%, poor offset stability, high-temperature drift, precise magnetic sensors cannot be used because of the strong magnetic field on the

surface of the conductor and it is highly dependent on the busbar orientation. Hall sensors and AMR are often used in this application. [16] presents the AMR sensor with the 300 A range, the linearity error below 1% and with no magnetic hysteresis. Another yokeless configuration is the circular sensor array with more than four sensors around the conductor, this configuration approximates the Ampère's law, and the accuracy of the measurement with an increasing number of the sensors is greatly increased. This setup brings better immunity to the external magnetic field [17, 18], and dependence on the conductor position [19]. The disadvantage of this solution is the bulky size that makes the sensor installation inaccessible at hard-to-reach places.

The configuration in which the transducer with a differential magnetic sensor inserted into flat busbar hole is used in this thesis. This setup allows us to measure the current with the range up to 1000 A and with linearity error lower than 0.1%. The advantage of this solution is simplicity, low-power consumption and low-cost. The principal disadvantages of this method are the crosstalk error which can be eliminated by using the configuration with more operating sensors (3x, 4x or 6x), and need for the drilling hole inside of the busbar. The other problem is frequency dependence due to non-uniform current distribution caused by the skin effect. [20] and [21] present a busbar with an amphitheater hole and a wedge bar, respectively. These methods significantly reduce frequency dependence from 14% with the cylindrical hole at 1 kHz to 9% with the amphitheater hole and to 3% with the wedge bar.

Three-phase current transducer with the magnetic sensors was presented recently in [22]. Authors use 6 AMR sensors Honeywell HMC1021 and calculate gradient for each of 3 pairs, where each pair measures the phase current in a distance of 30 mm. Suggested solution suppresses external homogeneous field, but does not suppress the field gradients. The first improvement was presented in [23] where we have used six microfluxgate sensors and suppression of the external disturbance was improved by 15 times than authors presented in [22].

In this thesis, I present the new method for measuring of the three-phase currents with the suppression of the external fields and field gradients up to second order using only six microfluxgate sensors. These sensors provide with an internal compensation coil to support a high-accuracy sensing range of ± 2 mT. The advantage of the used fluxgate sensor is low-offset, the low-crossfield error, that in our case has a significant meaning, the offset drift ± 5 $nT/°C$, low gain drift and of course one of the main advantages is the low price which is only 2.9$. [7]. The fluxgate sensors have advantages over almost all characteristics in comparison that are most commonly used in this field, namely, Hall sensors and AMR sensors; the precise AMR sensors have the small full-scale range (± 200 μT).

Chapter 2

Suggested new solution

This thesis focuses on the measurement of the AC and DC currents in three copper busbars by yokeless current transducers. Our current transducer with a range of 1000 A is based on two microfluxgate sensors TI DRV425 with the distance 2.5 mm, placed in the 19 mm diameter hole drilled in the center of each busbar as shown in Figure 2.1. Detailed picture of the PCB will be presented later (Section 2.3). The range of the current transducer for the particular application can be easily optimized via busbar geometry, size of the hole and distance between two DRV425 sensors. Six microfluxgate sensors are used in our configuration (two in each busbar, the distance between the centers of the busbars is 160 mm, the cross-section of each busbar is 60x10 mm) as shown in Figure 2.2. If we measure each current phase separately, we observe large crosstalk error, i.e., sensitivity to currents in the other phases and external currents and generally external fields.

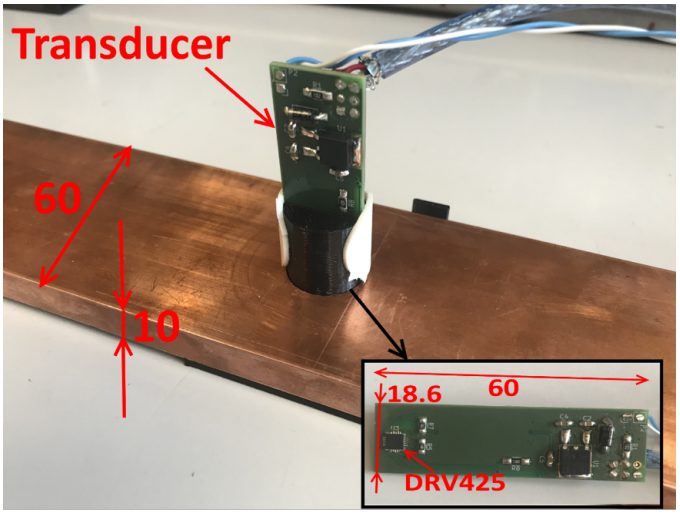

Figure 2.1: One of the three busbars with the transducer in the working position

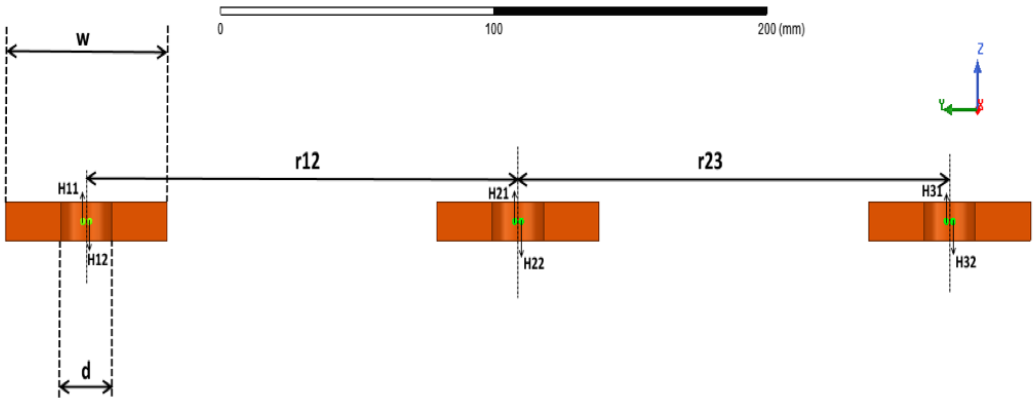

Figure 2.2: 2D Schematic of the configuration with the sensor placement inside the drilled holes. Green dots are the sensors with the labeled sensitivity axes.

2.1 Theoretical framework

The theoretical framework for the analytical model is developed. The Ampère's law is used for analytical calculation of the parasitic response to the external current; the current is localised to one point in this case. For the differential sensor with the spacing of 2a, the parasitic response to the idealized external current I in the distance of d in the same plane is

$$H_1 - H_2 = \frac{I}{\pi \cdot (d + 2a)d} \tag{2.1}$$

The busbars are also simplified for long distances as one point. The magnetic field calculated analytically and simulated 2D and 3D FEM models are compared, and results are shown in Figure 2.3.

The general equation for the six sensors is shown below. The system is overdetermined because of the four unknown components (three-phase currents and external disturbing current in line with the used conductors) and six sensors.

$$\begin{pmatrix} H_1 \\ H_2 \\ H_3 \\ H_4 \\ H_5 \\ H_6 \end{pmatrix} = \begin{pmatrix} -\alpha & \frac{1}{2\pi(r_{12}+a)} & \frac{1}{2\pi(r_{13}+a)} & \frac{1}{2\pi(r_{ext}+r_{13}+a)} \\ \alpha & \frac{1}{2\pi(r_{12}-a)} & \frac{1}{2\pi(r_{13}-a)} & \frac{1}{2\pi(r_{ext}+r_{13}+a)} \\ -\frac{1}{2\pi(r_{12}-a)} & -\alpha & \frac{1}{2\pi(r_{23}+a)} & \frac{1}{2\pi(r_{ext}+r_{23}+a)} \\ -\frac{1}{2\pi(r_{12}+a)} & \alpha & \frac{1}{2\pi(r_{23}-a)} & \frac{1}{2\pi(r_{ext}+r_{23}-a)} \\ -\frac{1}{2\pi(r_{13}-a)} & -\frac{1}{2\pi(r_{12}-a)} & -\alpha & \frac{1}{2\pi(r_{ext}+a)} \\ -\frac{1}{2\pi(r_{13}+a)} & -\frac{1}{2\pi(r_{12}+a)} & \alpha & \frac{1}{2\pi(r_{ext}-a)} \end{pmatrix} \begin{pmatrix} I_1 \\ I_2 \\ I_3 \\ I_{ext} \end{pmatrix} \tag{2.2}$$

where α is the current sensitivity of each sensor which depends on its distance from the center of the busbar, a is the distance from the center of the busbar to the microfluxgate sensor, r_{12} and r_{23} are denoted in Figure 2.2, r_{ext} is the distance to the external current, I_1, I_2, I_3 are the amplitudes of

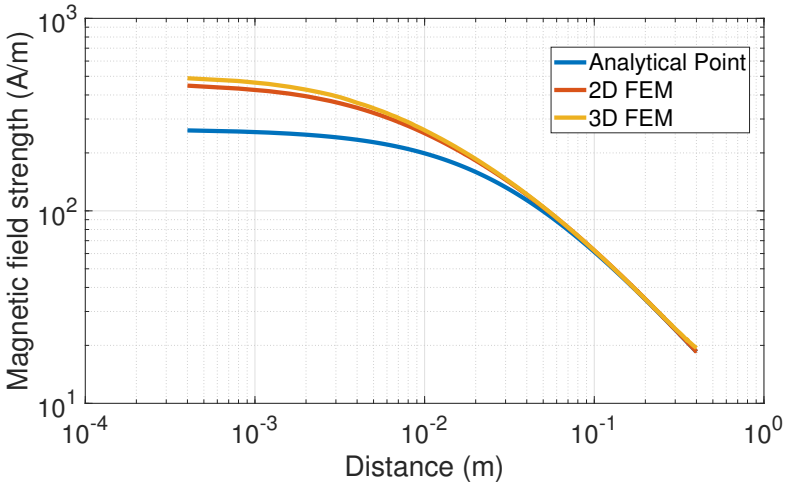

Figure 2.3: Comparison of the analytical, 2D and 3D FEM simulation, Flowing current I = 50 A

the three-phase currents, I_{ext} is the amplitude of the external current and $H_1, \ldots, H_6$ are the measured values by the corresponding sensors. If the distance to the external current is unknown, then the system is nonlinear and should be solved numerically, which is not practical for industrial applications. (2.2) gives the same approximation as the model in 3D FEM only for a distance 0.1 m and more as shown in Figure 2.3. This can be improved by the analytical formula for the rectangular conductor as shown in [24].

2.1.1 Magnetic field around the rectangular conductor

The magnetic vector potential is used for this analytical solution. Ampère's Circuital Law in point form for static fields follows

$$\nabla \times H = J \tag{2.3}$$

where H is the magnetic field strength, J is the current density and ∇ is the nabla operator.

The magnetic field B can be obtained from the curl of the magnetic vector potential defined by following

$$\nabla \times A = B \tag{2.4}$$

where A is the magnetic vector potential and $\nabla \cdot A = 0$ by definition. Using well-known ratio $H = \frac{B}{\mu}$, this gives us following:

$$\nabla \times (\nabla \times A) = \mu J \tag{2.5}$$

then $\nabla^2 A = -\mu J$, where $\mu = \mu_r \mu_0$ is the magnetic permeability, $\mu_0 = 4\pi \cdot 10^{-7}$ H/m and μ_r is the relative magnetic permeability of the material.

This can be rewritten as the Poisson's equation (if J=0 then it forms the Laplace's equation)

$$\frac{\partial^2 A}{\partial x^2} + \frac{\partial^2 A}{\partial y^2} = -\mu_r \mu_0 J \tag{2.6}$$

The busbar of rectangular cross-section is considered with the length of 2a = 60 mm and 2b = 10 mm. The current density J equals to $\frac{I}{4ab}$ for the flowing current I.

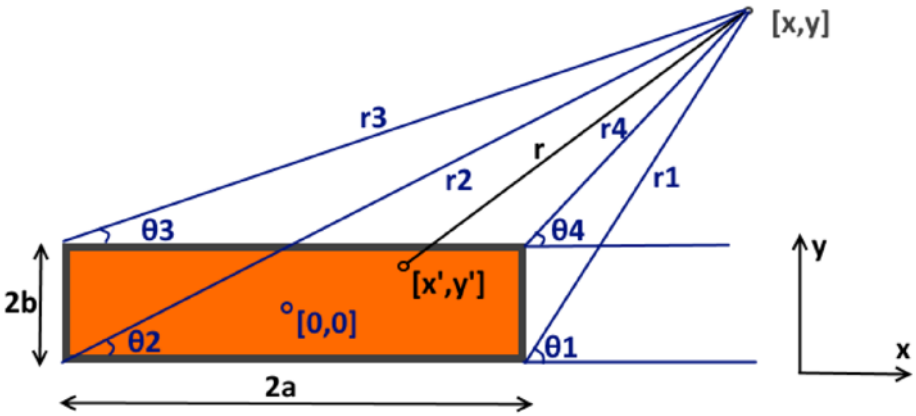

Figure 2.4: 2D theoretical schematic

We have arbitrary chosen point $[x', y']$ and the current i carried by this infinitely small cross-section $dx'\,dy'$ equals to $\frac{I}{4ab}\,dx'\,dy'$. After the integrating over the whole section of the our busbar at any point $[x', y']$, then

$$A = \frac{I\mu_0}{8\pi ab} \int_{-a}^{a} \int_{-b}^{b} \log r \, dx' \, dy' \tag{2.7}$$

If we substitute $r = \sqrt{(x'-x)^2 + (y'-y)^2}$, then it gives

$$A = \frac{I\mu_0}{16\pi ab} \int_{-a}^{a} \int_{-b}^{b} \log\left((x'-x)^2 + (y'-y)^2\right) dx' \, dy' \tag{2.8}$$

The result after the Strutt simplification as follows and shown in Matlab Contour plot in Figure 2.5.

$$
\begin{aligned}
A = \frac{I\mu_0}{16\pi ab}\{&(a-x)(b-y)\log((a-x)^2+(b-y)^2)+\\
&(a-x)(b+y)\log((a-x)^2+(b+y)^2)+\\
&(a+x)(b+y)\log((a+x)^2+(b+y)^2)+\\
&(a-x)^2(\arctan\frac{b-y}{a-x}+\arctan\frac{b+y}{a-x})+\\
&(a+x)^2(\arctan\frac{b-y}{a+x}+\arctan\frac{b+y}{a+x})+\\
&(b-y)^2(\arctan\frac{a-x}{b-y}+\arctan\frac{a+x}{b-y})+\\
&(b+y)^2(\arctan\frac{a-x}{b+y}+\arctan\frac{a+x}{b+y})\}
\end{aligned}
\tag{2.9}
$$

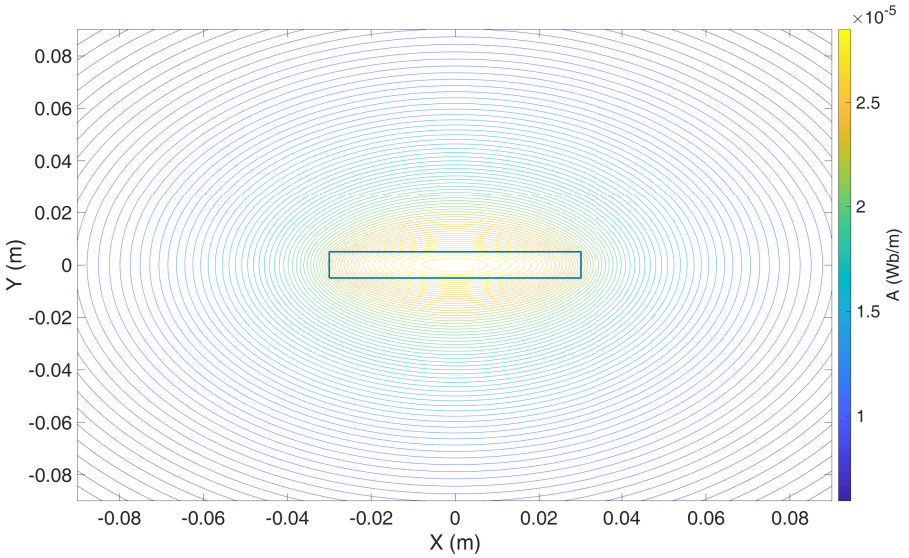

Figure 2.5: Magnetic flux lines, analytical solution

The magnetic field strength is then obtained using the vector potential with corresponding equations for x and y field components:

$$
H_x = \frac{1}{\mu_0}\frac{\partial A}{\partial y} \text{ and } H_y = -\frac{1}{\mu_0}\frac{\partial A}{\partial x} \tag{2.10}
$$

The deriving formula can be simplified by using θ_1, θ_2, θ_3, θ_4 and r_1, r_2, r_3, r_4 in accordance with Figure 2.4.

Then (2.10) gives

$$H_x = \frac{I}{8\pi ab}\{-(y-b)(\arctan\frac{x-a}{y-b} - \arctan\frac{x+a}{y-b}) - (y+b)(\arctan\frac{x-a}{y+b} + \arctan\frac{x+a}{y+b}) + (x+a)\log\frac{r_3}{r_2} - (x-a)\log\frac{r_4}{r_1}\} \tag{2.11}$$

$$H_y = \frac{I}{8\pi ab}\{-(x-a)(\arctan\frac{y-b}{x-a} - \arctan\frac{y+b}{x-a}) - (x+a)(-\arctan\frac{y-b}{x+a} + \arctan\frac{y+b}{x+a}) + (y+b)\log\frac{r_1}{r_2} - (y-b)\log\frac{r_4}{r_3}\} \tag{2.12}$$

where $r_1 = \sqrt{(x-a)^2+(y+b)^2}$, $r_2 = \sqrt{(x+a)^2+(y+b)^2}$, $r_3 = \sqrt{(x+a)^2+(y-b)^2}$ and $r_4 = \sqrt{(x-a)^2+(y-b)^2}$.

The equations (2.11) and (2.12) are the resulting equations which will be used for busbars contributions.

The resulting equations can be easily computed by the microprocessors and show us the better precision, especially for smaller distances as shown in Figure 2.6, the obtained results fully correspond to the 2D FEM simulation. The biggest difference is for 0.4 mm with corresponding error equals to the 9.3%, then the error is reduced to 3.7% at the distance 10 mm. The error for our configuration (for 160 mm distance between the centers of the busbar equals to 0.018%) and most likely caused by the inaccuracies in FEM simulations that can be easily solved by improving mesh, but time consumption is increased many times. The developed theoretical framework is confirmed, and it will be used for further calculations and analysis.

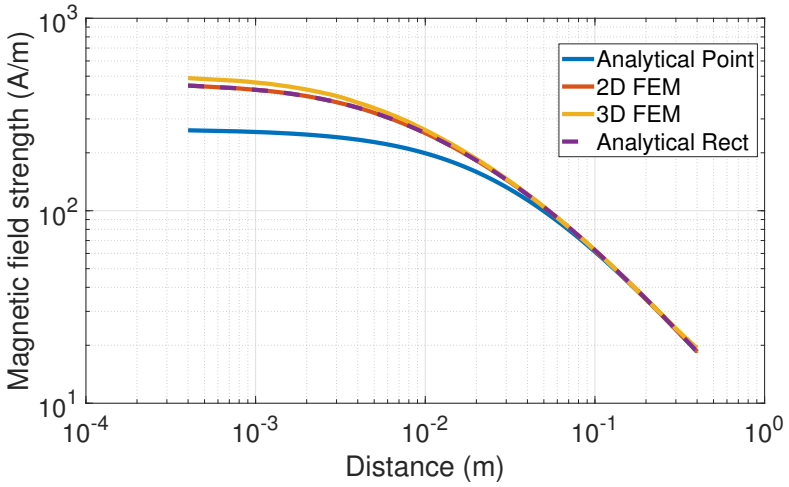

Figure 2.6: Flowing current I=50 A, comparison of all methods

2.2 Fluxgate sensors

Fluxgate sensors measure the magnitude and direction of the DC and low-frequency AC magnetic field in the range of 10^{-10} to 10^{-4} T. The ferromagnetic core is excited by the AC current of frequency f into the excitation winding. The core permeability $\mu(t)$, therefore, is changing with $2f$ frequency. If the measured DC field B_0 is present, the associated core flux $F(t)$ is also changing with $2f$, and voltage V_{ind} is induced in the pickup (measuring) coil having N turns as shown in Figure 2.7. The typical modern low-noise fluxgate magnetometer is the parallel type with a ring-core sensor, but double-rod sensors also have a lot of disadvantages. A phase-sensitive detector extracts the second harmonic in the induced voltage. Used microfluxgate sensor TI DRV425 consists of the single core, and other existing configurations as the double-rod sensor of Vacquier type or Forster type are shown in Figure 2.8 [6].

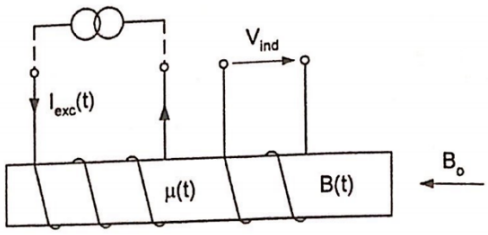

Figure 2.7: Basic fluxgate principle [6]

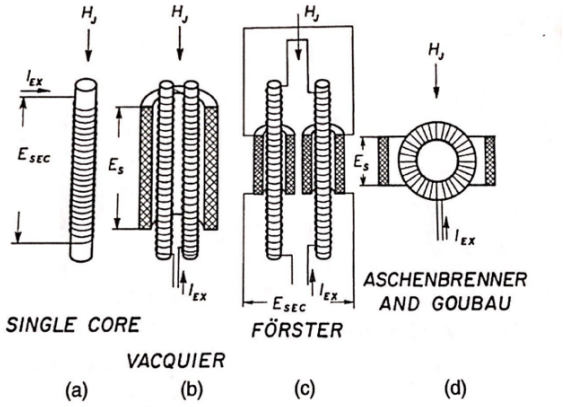

Figure 2.8: Different types of fluxgate magnetometer [6]

2.2.1 TI DRV425

The TI DRV425 [7] is a single-axis feedback compensated fluxgate magnetic sensor with the analog signal output which is proportional to the sensed magnetic field. The full range of the sensor is 2 mT, and it can be easily

changed by the shunt resistor, the only one component outside of the sensor. equation (2.13) shows the ratio how the shunt resistor (R_{shunt}) influences the measured magnetic field. The full-scale range for 100 Ω shunt resistor equals to ±500 μT. Therefore, for the higher magnetic field, the resistance of the shunt resistor should be decreased, and the current through R_{shunt} is increased. The output voltage of the differential amplifier will reach its peak amplitude with a maximum voltage drop across R_{shunt} as shown in (2.14).

$$H = \frac{1}{\mu_0} \frac{V_{out}}{4 \cdot 12.2 \cdot R_{shunt}} \tag{2.13}$$

where 4 V/V is the nominal gain $G_{nom} = \frac{V_{out}}{(V_{AINP} - V_{AINN})}$ (AINP and AINN non-inverting and inverting input of the shunt-sense amplifier, respectively) and 12.2 mA/mT is the gain G.

$$VR_1 = \frac{VDD - V_{ref}}{4} \tag{2.14}$$

The necessary electronics for measurement is on-chip, including the pick-up coil, compensation coil, difference amplifier, precision reference, and diagnostic functions to minimize component count and system-level cost. The functional block diagram is shown in Figure 2.9.

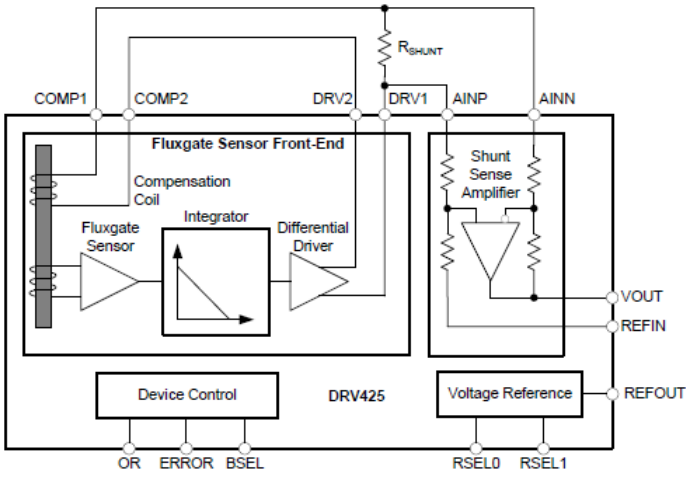

Figure 2.9: Functional Block Diagram of TI DRV425 [7]

As shown in the functional block diagram the fluxgate sensor consists of a magnetic fluxgate sensor with necessary sensor conditioning and compensation coil to internally close the control loop. The fluxgate sensor is repeatedly driven in and out of saturation and supports hysteresis-free operation with excellent accuracy. The internal compensation coil assures stable gain and high linearity. The magnetic field (B) is detected by the internal fluxgate sensor in the DRV425. The device integrates the sensor output to assure high-loop gain. The integrator output connects to the built-in differential driver that drives an opposing compensation current through the internal

compensation coil. The compensation coil generates an opposite magnetic field that brings the original magnetic field at the sensor back to zero. The compensation current is proportional to the external magnetic field, and its value is 12.2 mA/mT. This compensation current generates a voltage drop across an external shunt resistor, R_{SHUNT}. An integrated difference amplifier with a fixed gain of 4 V/V measures this voltage and generates an output voltage that is referenced to REFIN and is proportional to the magnetic field.

The main advantages of this sensor are the low-offset, offset drift, and noise of the sensor, combined with the precise gain, low gain drift and its high excitation frequency which gives a measurement bandwidth of 47 kHz. Low nonlinearity is given by the internal compensation coil and is shown in Figure 2.9. Analog output voltage in dependence of the busbar current is shown in Figure 2.10. The linearity error is below 0.1% for 60 A busbar current and shown in Figure 2.11. The sensor is miniature, its size equals to 4x4 mm and produced in WQFN package with power pad for optimized heat dissipation. These benefits explain why this sensor is selected for the current sensing application and ideal for our purpose.

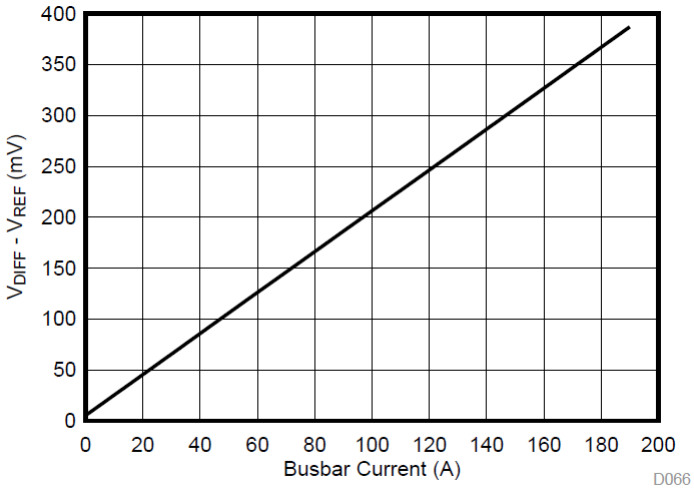

Figure 2.10: Analog Output Voltage vs Busbar Current [7]

2.3 Electrical connection of magnetometer

The electrical circuit was designed for the differential connection of the fluxgate sensors. The electrical circuit and PCB design were done in KiCad. The connection of the fluxgate sensor is shown in Figure 2.12. The bill of materials for this circuit is shown in Table 2.1.

R_2 is the 100 Ω shunt resistor which is used for changing the sensitivity and was described in Section TI DRV425. R_3 and R_4 are 10 kΩ pull-up resistors on the /OR (OverRange) and /ERROR flag output pins, respectively. The chip side of the resistor can be simply probed for observing the state of the flags. These pins are an open drain, and pull-up resistors are required to

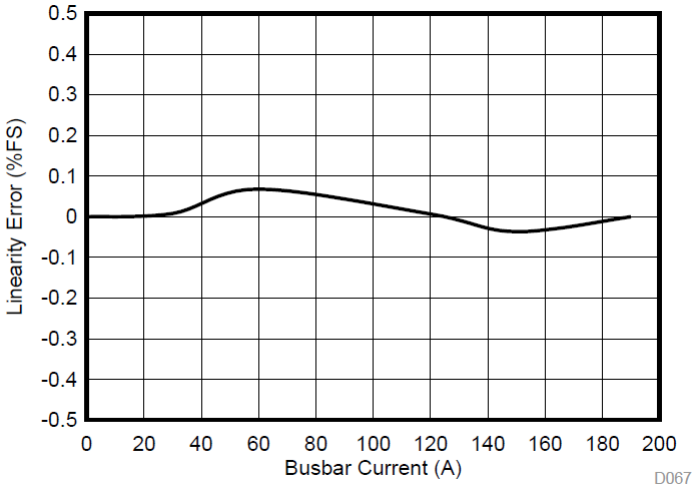

Figure 2.11: Linearity Error vs Busbar Current [7]

observe the active low output state. These pins may also be fly-wired to a microcontroller for use as interrupt pins. C_3 and C_4 are the decoupling capacitors, and they suppress the high-frequency noise in power supply signals. The RSEL0 and RSEL1 pins are connected to the power supply to have the ratio-metric reference which is equal to VDD/2, in this case, the maximum offset of the magnetometer according to the datasheet equals to ± 8 μT. If RSEL0 and RSEL1 are connected to the ground, the sensor degrades to $\pm$ 18 μT, because if V_{ref} is unknown (2.5 V $\pm$ 50 mV), then the offset

$$B_{offset} = \pm 8 \text{ uT} + \frac{50 \text{ mV}}{100\ \Omega \cdot 12.2 \text{ mA/mT} \cdot 4 \text{ V/V}} = \pm 18\text{uT} \qquad (2.15)$$

Designation	Description
R2	SMD Resistor R0805, 100R, 1%, 0.125 W, 100ppm/K, YAGEO
R3, R4	SMR Resistor R0805, 10k, 1%, 0.125 W, 100ppm/K, YAGEO
C3, C4	Ceramic capacitor SMD 0805, 1u/25V, X7R, 10%, YAGEO
U1	Fluxgate Magnetic field sensor TI DRV425

Table 2.1: Bill of materials DRV425

Overall connection of the sensor for one transducer is shown in Figure 2.13. This electrical circuit has the diode D2 which serves as the protection against the reverse voltage, capacitors C_1 and C_2 are output and input decoupling capacitors, respectively. They provide a low-impedance high-frequency path at the input and the output of the linear voltage regulator U_2. Both are needed and recommended to suppress high-frequency noise from the source and from the load, to avoid bounce on the regulated voltage to achieve electromagnetic compatibility (EMC). The output capacitor is also required for frequency compensation (i.e., to avoid instability of the linear regulator). D_1 is the LED which serves as the indicator that the circuit is powered, R_1

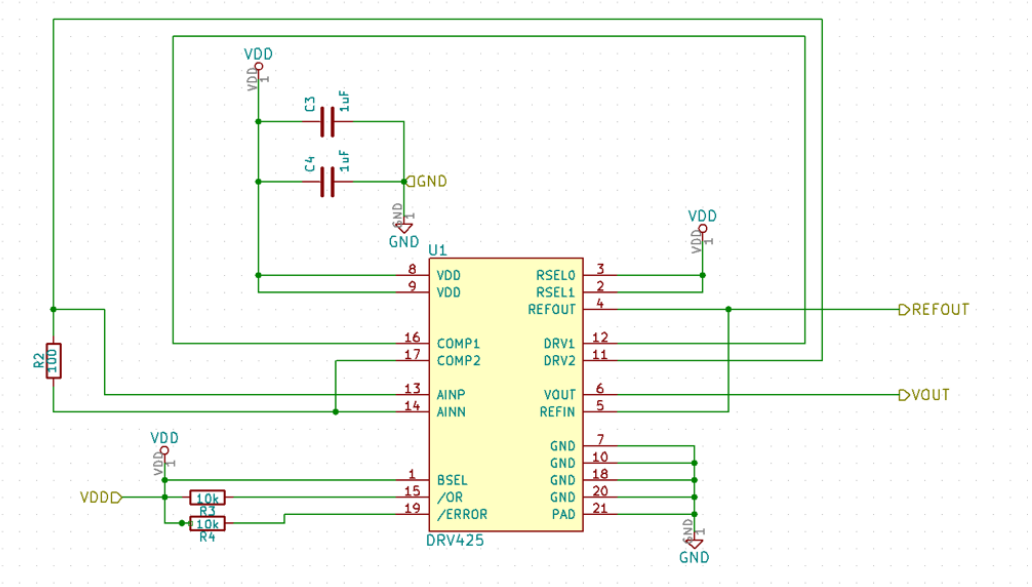

Figure 2.12: Electrical connection of DRV425

is the current limiting resistor. R_8 and R_9 are the 100 Ω decoupling resistors on the difference amplifier output, which prevent the start of oscillations (identical to phase enhancement) and serve to avoid the instability of the output signal. J_1 and J_2 are the generic connectors, double and single row, respectively. J_1 is used for taking output signal and reference signal of the sensors, and J_2 serves as the power supply connector. Power flags are used to indicate that the power is supplied from the external source. The bill of materials for the overall connection is shown in Table 2.2.

Designation	Description
R1	SMD Resistor R0805, 1k0, 5%, 0.25 W, 100ppm/K, YAGEO
R8, R9	SMD Resistor R1206, 100R, 1%, 0.25 W, 100ppm/K, YAGEO
C1, C2	Ceramic capacitor SMD 0805, 1u/25V, X7R, 10%, YAGEO
D1	LED 1206, YELLOW, 120°, 150 mcd at 20 mA, $\lambda = 592$ nm
D2	Diode 1N4007
U2	Voltage Regulator, TO-263, SMD 7805, D2PAK, 5V, 1.5A

Table 2.2: Bill of materials, Overall Connection

PCB board was designed, which has a width of 18.6 mm and a height of 60 mm. The Front and Back copper layers are shown in Figure 2.14. The fluxgate sensors are located in the way to have their axes of sensitivity (between pin 1/15 according to the datasheet [7] in the same place but on the opposite sides of the PCB. The 3D models of the PCB from the front and back view are shown in Figure 2.15.

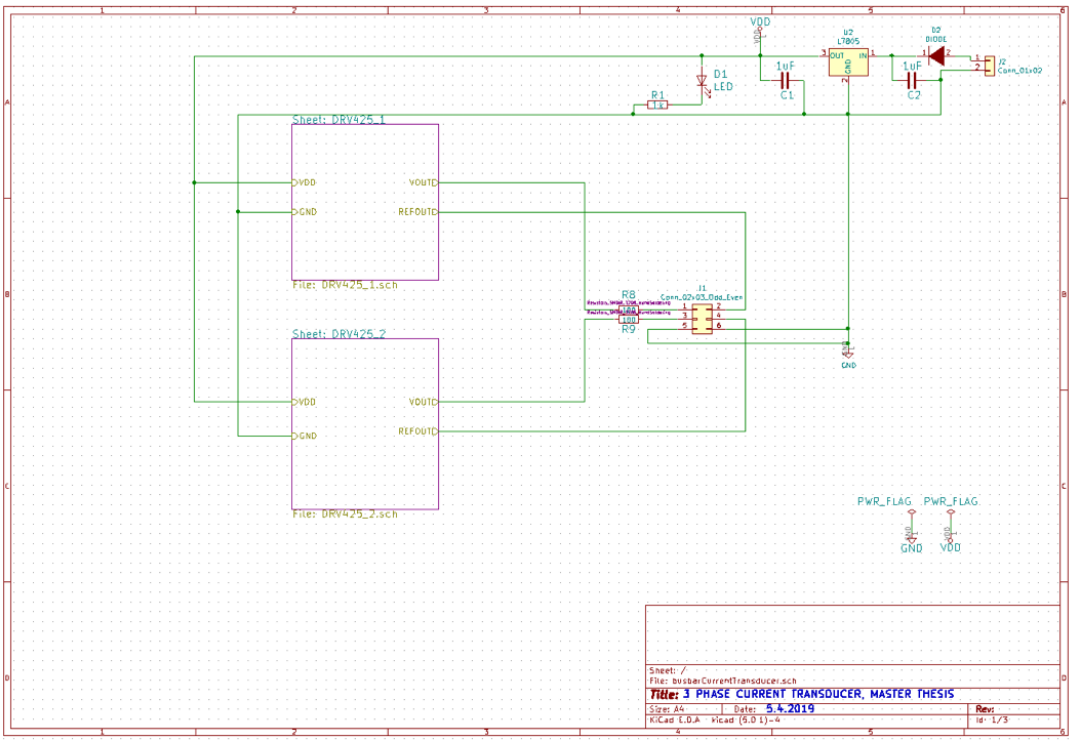

F

Figure 2.13: Electrical Connection of two magnetometers

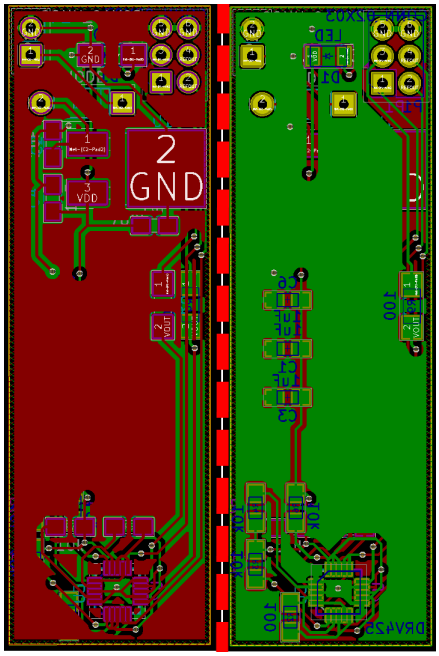

Figure 2.14: Left - Front copper layer, Right - Back copper layer

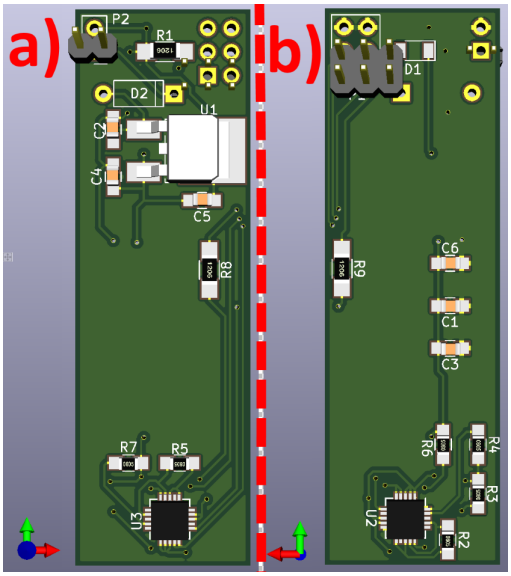

Figure 2.15: a) Front view of the PCB b) Back view of the PCB

Chapter 3

FEM simulation

The pair of the microfluxgate sensors are inserted into the cylindrical 19 mm hole in the 60x10 mm copper busbar. For the distance between the sensors of 2.5 mm, the sensitivity to DC measured current calculated by FEM is s= 1.6 (A/m) / A, this value was also verified experimentally. For 50 A DC current H_{FEM} = 81 A/m,H_{Meas}= 80 A/m. For AC current the current distribution is no longer uniform due to the eddy current, and the sensitivity drops down with frequency. Comparison of the current distribution in the busbar at 50 Hz and 1 kHz is shown in Figure 3.1, the comparison of the magnetic field strength inside the drilled hole is shown in Figure 3.2.

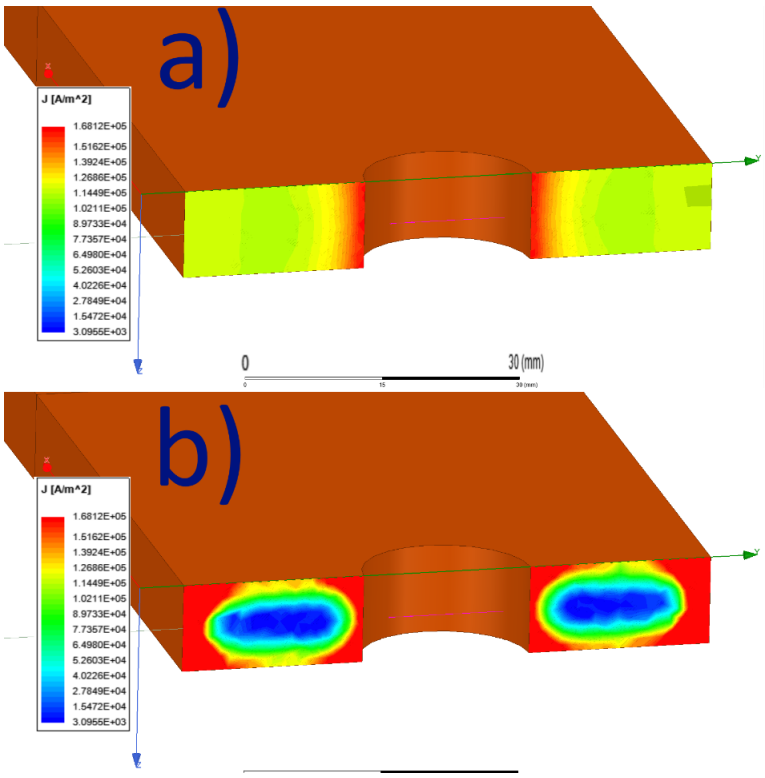

Figure 3.1: Current distribution a) 50 Hz b) 1 kHz

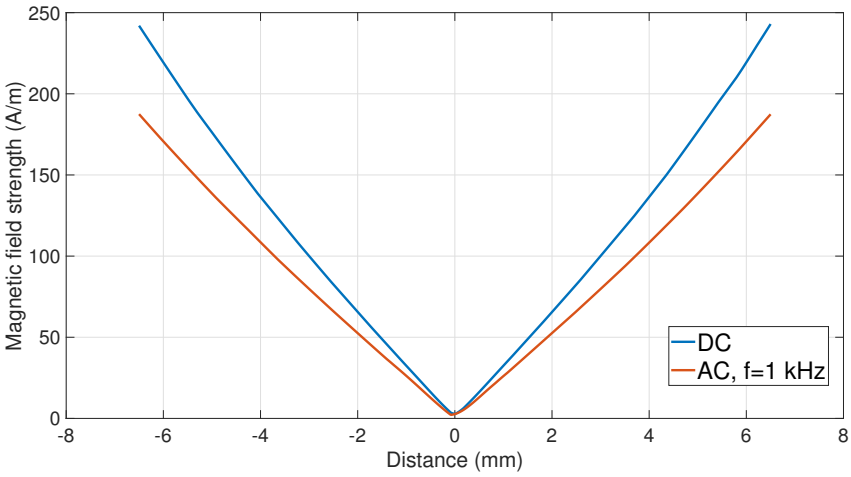

Figure 3.2: Magnetic field strength inside the hole, 0 mm corresponds to the center of the busbar

3.1 Skin Effect

Skin effect is the tendency for AC current to concentrate near the outer part or "skin" of a conductor. For a steady unidirectional current through a homogeneous conductor, the current distribution is uniform over the cross-section; that is, the current density is the same at all points in the cross-section. With an alternating current, the current is displaced more and more to the surface as the frequency increases. The conductor's effective cross section is therefore reduced, so the resistance and energy dissipation is increased compared with the values for a uniformly distributed current. The effective resistance of a wire rises significantly with frequency; for example, for a copper wire of 1-mm diameter, the resistance at a frequency of 1 MHz is almost four times the DC value [25].

A mathematical description of skin effect can be derived from Maxwell's equations, but exact solutions have been obtained for only several simple shapes, including cylindrical, tubular, and flat conductors. For a plane conductor carrying a sinusoidal alternating current, the current density is a maximum at the surface, and its magnitude decreases exponentially with distance into the conductor. A skin depth or penetration depth δ is frequently used in assessing the results of skin effect; it is the depth below the conductor surface at which the current density has decreased to $1/e$ (approximately 37%) of its value at the surface and is given by (3.1).

$$\delta = \sqrt{\frac{1}{\pi f \mu \sigma}} \tag{3.1}$$

where f is the frequency and σ and μ are the conductivity and permeability of the material, respectively. This concept applies strictly only to plane solids, but can be extended to other shapes provided the radius of curvature of the

conductor surface is appreciably higher than δ.

At a frequency of 50 Hz the penetration depth in copper ($\sigma = 5.55 \times 10^7$ Sm^{-1}, $\mu = 4\pi \times 10^{-7}$) is found from the above expression to be 9.55 mm; at 1 kHz it is 2.14 mm and at 1 MHz it is only 67.56 μm.

Waveguide and resonant cavity internal surfaces for use at microwave frequencies are therefore frequently plated with a high-conductivity material, such as silver, to reduce the energy losses since nearly all the current is concentrated at the surface. Provided the plating material is thick compared to δ, the conductor is as good as a solid conductor of the coating material. [25]

3.2 FEM model

Three copper busbars which correspond to the real ones are modeled in ANSYS Maxwell. The 3D - model is shown in Figure 3.3. The distance between the centers of the busbars is 160 mm. The electrical conductivity of the copper was measured using the four-terminal method with the measuring DC current of 50 A in the region of homogeneous current density. The odd symmetry is applied to the center cross-section of the busbars for reducing computational time. Time step in the transient simulation equals to 250 μs that corresponds to 80 samples per one period. The current in each phase is shown in Figure 3.4.

The fourth busbar with the same dimensions is modeled as the source of the external disturbance, and his influence is examined. The parasitic response to the external lateral disturbance (in-plane 5A current) as the function of the distance is shown in Figure 3.5. The reading error for the minimum external distance of 10 mm for the measured current, which is the closest to the disturbance equals to 35% without compensation and to 4% with compensation. If we calculate the current based on the data from the sensors without additional processing, the error for the current is much higher, and it is necessary to use the post-processing of the signals. Based on Figure 3.5, it is argued that the compensation method reduces the reading error ten times on the average in the comparison with non-compensated method.

For the current which is outside the plane (superior current), the situation is not much better. For the superior disturbance, the differential pair of sensors does not suppress disturbance anymore. The external modeled busbar is located above the middle busbar, and the external distance, in this case, is the distance from the center of the middle busbar to the center of the external busbar. The results of the simulation for the superior case are shown in Figure 3.6. Reading error for the middle busbar I_2 is large for small distances, i.e. for 5 mm the error for uncompensated method is 67%, but for compensated method it is 6.5%; For the side currents I_1 and I_3: error for the uncompensated method is 16% and for compensated is 3%, again the reading error is greatly reduced by the compensation method.

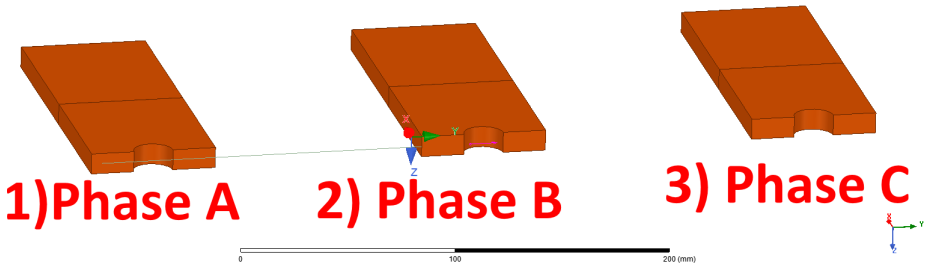

Figure 3.3: 3D FEM Model in ANSYS

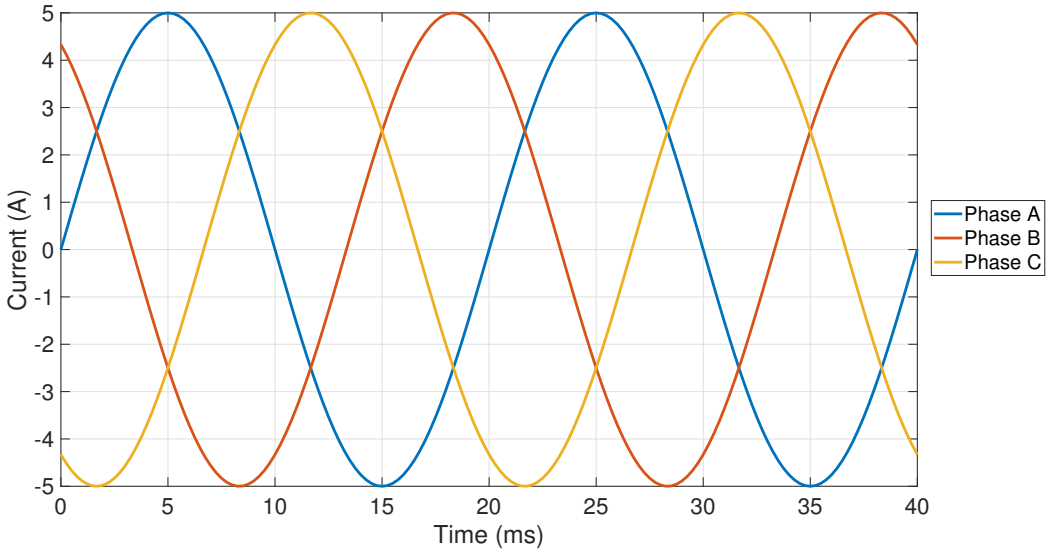

Figure 3.4: Current in each phase

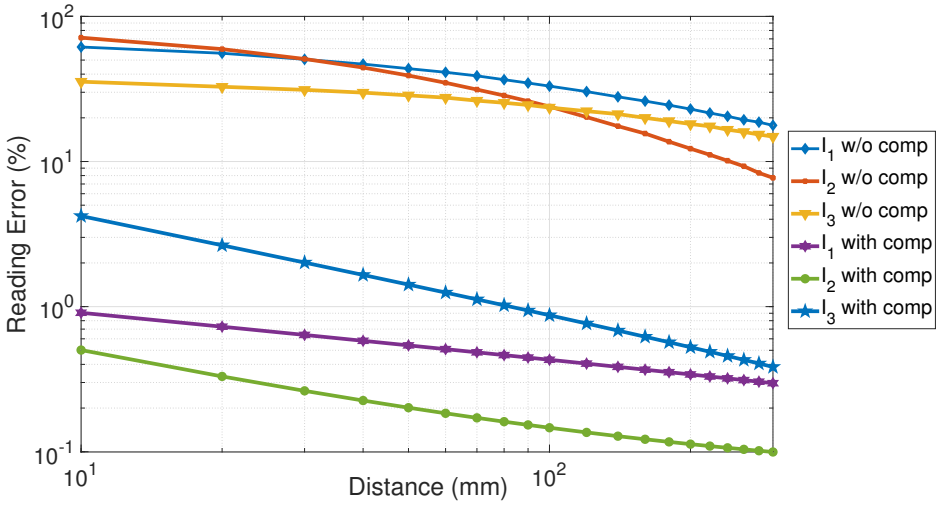

Figure 3.5: Reading error for each current with compensation and without as a function of the distance for lateral disturbance

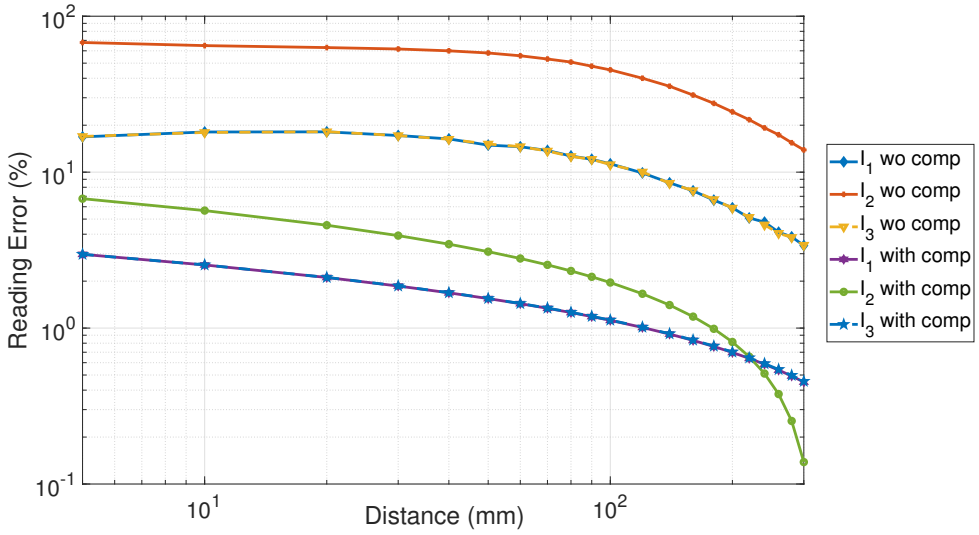

Figure 3.6: Reading error for each current with compensation and without as a function of the distance for superior disturbance

Chapter 4

Measurement

The Wye (or "star") configuration is used for the measurement. This configuration has three loads connected at a single neutral point. The connection scheme is shown in Figure 4.1, where B1, B2, B3 are the 3 copper busbars; R1, R2, R3 are the rheostats (6.3 A, 13 Ω) which are used in the circuit to control the flowing current, and R4, R5, R6 are the reference 0.01 Ω resistors which are used as the shunt resistors. The three-phase transformer 220 V to 40 V is used to reduce the voltage and shown in Figure 4.1. For the external current the transformer 220 V / 24 V is used, and the external current is in-phase with L2. The signals from the sensors are processed by multifunctional DAQ-Card NI-USB 6211, and LabVIEW program is described in the next section.

The sample rate for the measurement is set to 10 kHz, and the differential connection between the V_{out} and V_{ref} is used for obtaining the magnetic field strength. The measured values are saved in the .txt files, and the raw data are used in the post-processing in Matlab.

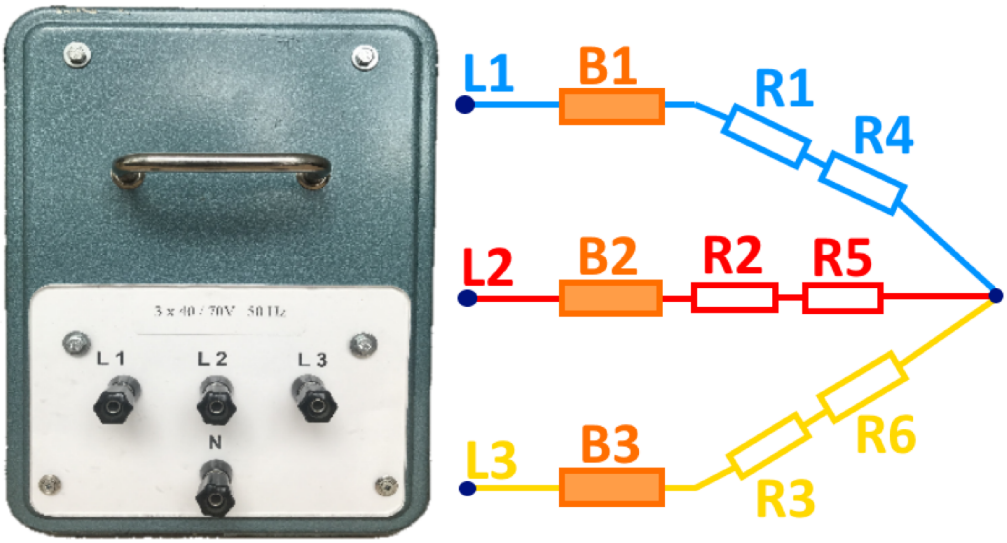

Figure 4.1: Electrical Connection

4.1 LabVIEW program

The control program is created in LabVIEW for processing the data from the sensors and computing the currents. The control window is shown in 4.2. The analog input channels which are connected to the magnetometers outputs, maximum and minimum voltage settings, sample clock source, terminal configuration (differential is used by default) are chosen in the "Configuration" section at the top left. The section "Log files" is used for logging data from the sensors, both filtered values (mean and RMS) and raw data. Raw data are shown in the plot "Analog signals from the sensor" and saved to a .txt file with the prefix which is set in "File Prefix Save sensors 2" control button, the base to this file is chosen under this button. 5000 values are saved with the current settings for each sensor in the six columns. The same buttons above are used for saving filtered values with the measurement parameter to a .txt file. The chosen parameter can be any number, either the distance to the disturbance or the RMS of the external current and is set in "Parameter (-)" control button.

The instantaneous output signal from the sensors in mV, DC component, and computed RMS component are shown in the "Measured data" section. The measured current is obtained by measuring the voltages on the reference 0.01 Ω resistors and also displayed in this section on the right side. Two plots are on the right side with the black background, which show the Mean (upper) and RMS (below) values from the sensors in dependence on the time.

Finally, the four buttons at the bottom are used for control and saving data. The 1st button "Write to file" is used for the saving Mean, RMS, and parameter values. The 2nd is used to clear the charts with the black background (Mean and RMS values vs. Time). The 3rd button is used for saving raw data, and the 4th is used to remove the offsets of the sensors.

NOTE: The offset button should be used when the sensors are placed in the multi-layer Permalloy shielding to isolate them from the external magnetic field.

The LabVIEW program should be stopped by the "STOP" button at the end of the measurement.

4.2 Sensor holder

The readings of our transducers are highly dependent on the position inside the busbar. The holder for each sensor was designed, and the 3D model with denoted dimensions in AutoDesk is shown in Figure 4.3. The dimensions of the base part are 62x45x2 mm, with the side parts having a width of 2 mm. The diameter of the cylinder is 19 mm, and the hole in it has a width of 3.7 mm. The holder was produced on a 3D printer and made of black polycarbonate-ABS, one of the most widely used industrial thermoplastics.

The holder is designed so that the axis of the sensitivity for both sensors corresponds to the middle of the busbar when the transducer is fully inserted

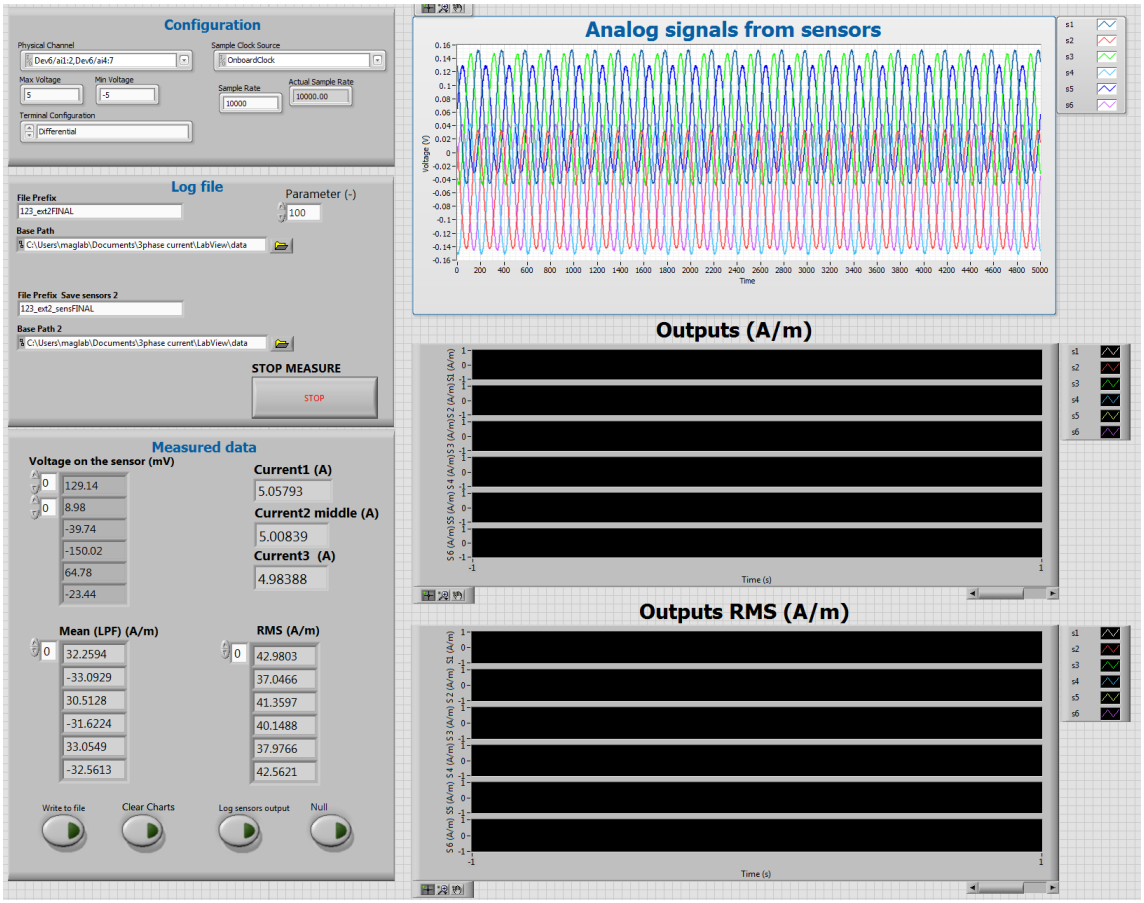

Figure 4.2: LabVIEW control program

into the cylinder's hole and securely fixed inside. The side parts securely fix the sensor and prevent the holder from rotating.

4.3 Calibration of the sensors

The calibration for each sensor is performed to reduce the error, which is caused by the incorrect sensitivity coefficients. Sensors were placed in Helmholtz coil with the calibration constant 20.44 (A/m)/A. The 5 A current was applied by the DC power supply Agilent 6632B, that corresponds to 102.2 A/m. The commutation is done for the eliminating of the DC component of the magnetic field. Calibration coefficient for each sensor is shown in Table 4.1. All calibrations coefficients are applied to the program in LabVIEW and automatically multiply the outputs from the sensors.

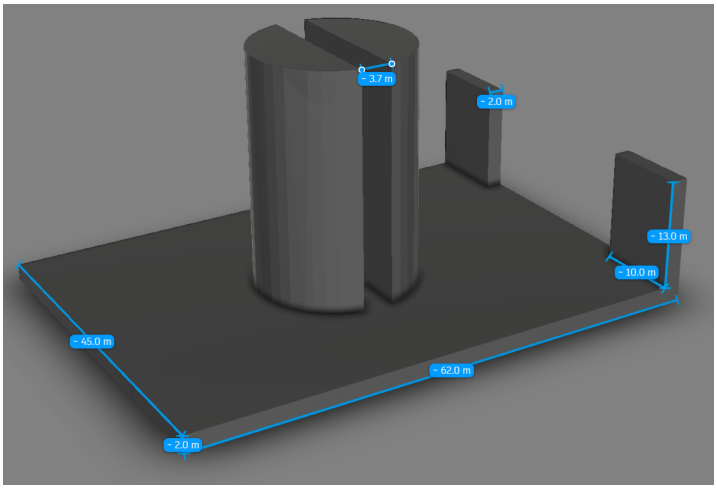

Figure 4.3: 3D model of the holder

№of Sensor	Calibration coefficient
1	1.005
2	0.985
3	1.01
4	1.006
5	1.012
6	0.99

Table 4.1: Calibration coefficients for each sensor

4.4 Measurement

Experimental set-up for the lateral and superior case is shown in Figure 4.4. The rheostats and the reference resistors are shown in Figure 4.5. The sensors are supplied by 7 V by GoldStar DC power supply GP-305. The comparison of FEM simulation and the results of the measurement is shown in Figure 4.6 for the lateral case. The 3 A_{rms} current flowing through the three busbars is read by the software for better precision and accuracy of the measurement with 10 kHz sample frequency. The data are post-processed offline. The maximum difference for the lateral case between the measurement and simulation is 1.5%. Therefore, we can state, that the simulation is confirmed by the experiment.

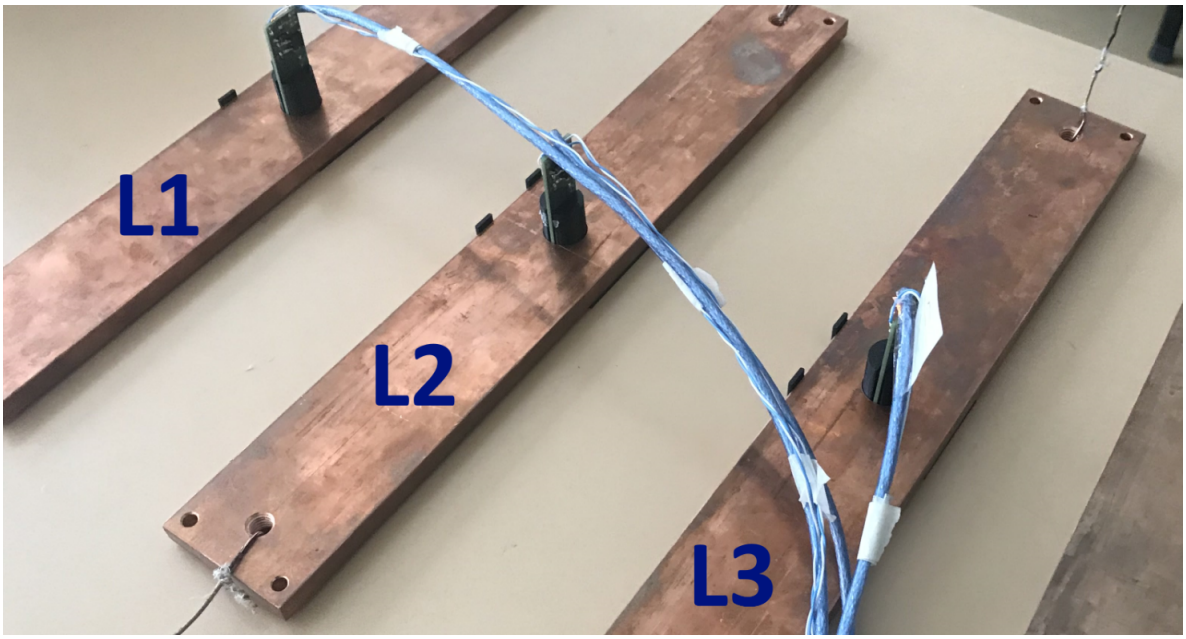

Figure 4.4: Three busbars - Experimental set-up

Figure 4.5: Rheostats and the reference 0.01 Ω resistors

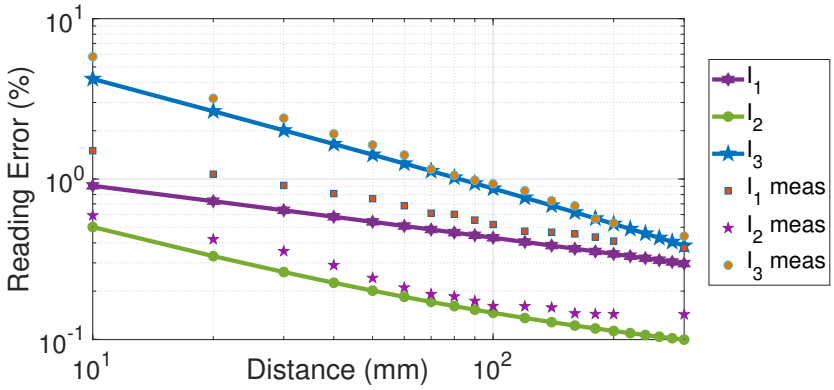

Figure 4.6: Comparison of the simulation result and the measurements

Chapter 5

Rectangular current transducer

A new method for measuring the current in the busbars was suggested in CTU in 2016 [8]. This method uses 16 microflugate sensors TI DRV425 to better approximate the closed integral and, therefore, uses the Ampère's law. Theoretically, an infinite number of the sensors around the conductor gives us the ideal current calculation and great immunity to the external currents. The microfluxgate sensors are placed in the circumference of the aluminum conductor, which has the 100x10 mm cross-section, their location around the conductor is shown in Figure 5.1. The full-scale range for this type of the transducer is ±400 A. Such type of the conductors (aluminum busbar with the cross-section 100x10 mm) is used in power stations as the grounding conductors as shown in Figure 5.2. Their advantage is that they are made of non-magnetic materials; otherwise, the transducer should be calibrated again due to the magnetic properties of the material [26]. The picture of the transducer from the top side is shown in Figure 5.3. The dimensions of the transducer are as follows: 104 x 14 mm, that makes the sensor compact in comparison with [27], where the circular array is used which has the bulk size and being inappropriate for installation in hard-to-reach places. The weight for each sensor output is defined by means of FEM simulation in ANSYS Maxwell. The transducer is compared with the commercially available standard LEM HOP-800SB. The industrial standard uses 2 Hall sensors installed in the airgaps of the magnetic yoke, which is used for the concentration of the magnetic flux, and the transducer operates without feedback compensation. This type of sensor was the only meaningful alternative available on the market for this type of the busbar.

- Same weights method
  Each sensor has the same weight w (A/(A/m)). For DC current the weight for each sensor equals to 0.0147 A/(A/m). Then the total current in the conductor calculated by (5.1).

$$\begin{aligned} w =& w_1 = w_2 = w_3 = \ldots = w_i = \ldots = w_{16} \\ I_{total} =& w(H_1 + H_2 + H_3 + \ldots + H_i + \ldots + H_{16}) \end{aligned} \tag{5.1}$$

  where I_{total} is the flowing current in the conductor and $H_1,\ H_i, \ldots, H_{16}$ are the measured values by the i-th microfluxgate sensor.

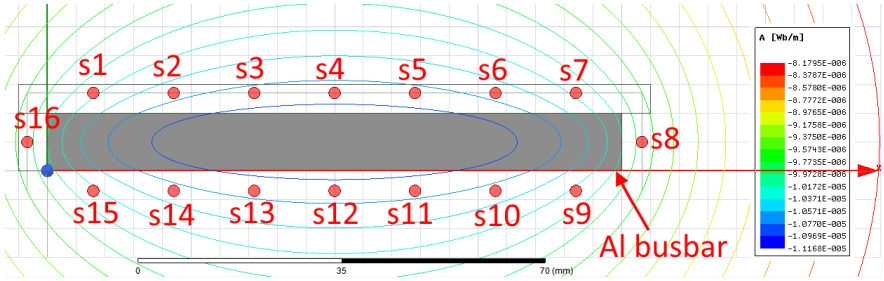

Figure 5.1: Distribution of the microfluxgate sensors around the busbar conductor [8]

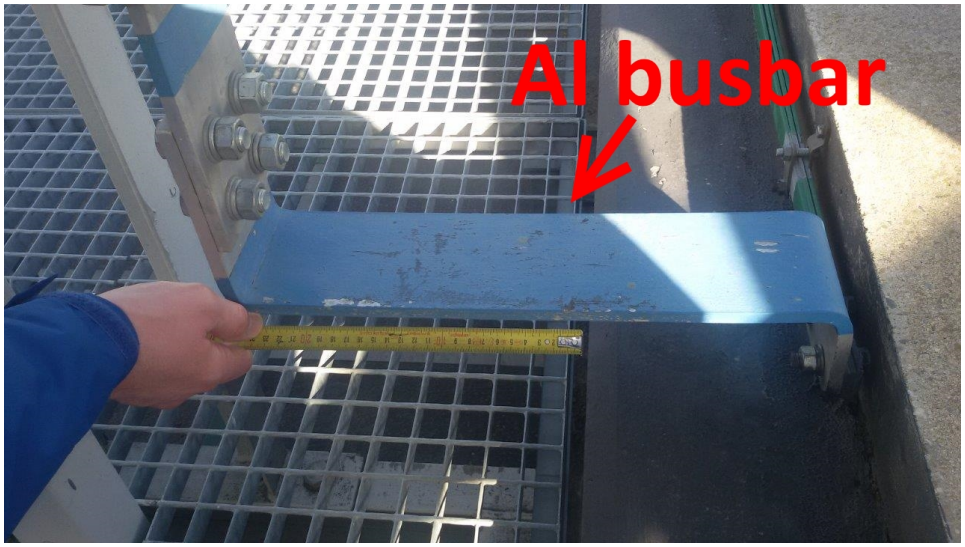

Figure 5.2: Al busbar as the grounding conductor at Mírovka distribution station

- Integral method
  The circumference of the busbar is divided into separate sections for each sensor; therefore, each sensor has its weight. Tangent component of the magnetic field is calculated in each section at a distance 3.5 mm from the surface of the conductor which corresponds to the real distance of the sensor and then numerically integrated in Matlab using Trapezoidal numerical integration. The obtained value is divided by the magnetic field strength which is computed in the place of the particular sensor (5.2).

$$\begin{aligned} w_i &= \frac{\int_C H_{tangential}\, ds}{H_{iFEM}} \\ I_{total} &= (w_1 H_1 + w_2 H_2 + \ldots + w_i H_i + \ldots + w_{16} H_{16}) \end{aligned} \tag{5.2}$$

- Weighted method

  This method also utilizes coefficients for each sensor. The particular coefficients are obtained by dividing the flowing current in the simulation by the magnetic field strength, which is computed in the place of the

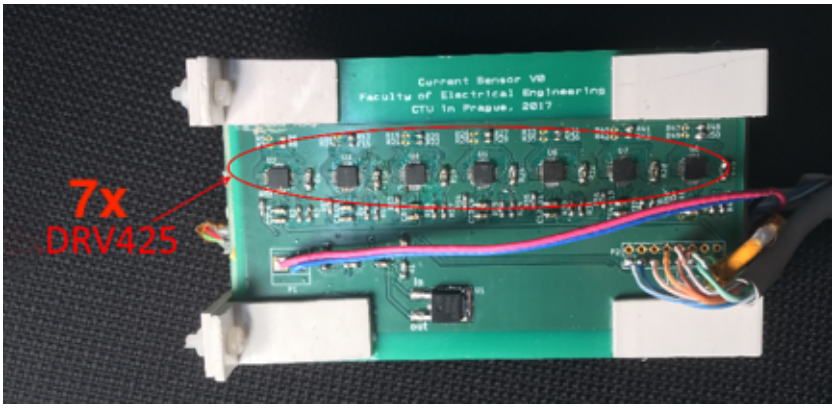

Figure 5.3: Picture of the yokeless current transducer with the 16 integrated microfluxgate sensors [8]

particular sensor. The total current is the average of the multiplication of the weight and measured magnetic field strength for each sensor (5.3).

$$\begin{aligned} w_i &= \frac{I_{FEM}}{H_{iFEM}} \\ I_{total} &= \frac{w_1 H_1 + w_2 H_2 + \ldots + w_i H_i + \ldots + w_{16} H_{16}}{16} \end{aligned} \tag{5.3}$$

5.1 Temperature stability

Temperature stability is calculated for three different methods which are described above and for LEM HOP-800SB, industrial standard sensor. The LEM HOP-800SB operates without feedback compensation and, therefore, the worse values for the temperature stability are expected.

The temperature stability is calculated for three different temperatures in a wide range. The temperature is measured by the K-type thermocouple wired to Thermometer Lutron TM2000. The sensors were cooled in the freezer and heated in the LabNet I5110A, mini incubator. The measured current offsets for three methods and LEM HOP-800SB are shown in Table 5.1 and 5.2, respectively. The calculated temperature drifts for the LEM and yokeless transducer are shown in Table 5.3.

Temp. (°C)	**Offset (mA)**		
	Same weights	**Int. method**	**Weighted method**
-11	-301	249	389
25.3	220	193	305
55	99	92.24	182.4

Table 5.1: Our transducer: offset as the function of the temperature [8]

Temperature (°C)	Offset (mA)
-22.2	2850
25.3	840
59.9	-1104.9

Table 5.2: LEM HOP-800SB: offset as the function of the temperature [8]

Parameters	LEM HOP 800-SB	Yokeless transducer		
		Same weights	Integral method	Weighted method
FS range (A)	800	400		
Drift (mA/(°C))	48.1	3.06	3.13	2.37
Drift (%FS/(°C))	6e-3	7.65e-4	7.83e-4	5.93e-4

Table 5.3: Offset temperature drifts calculated for LEM and yokeless transducer [8]

5.2 Noise

Another property that was compared is the noise of the current measurement. The LEM transducer was analyzed by FFT Spectrum Analyzer SR770 and the our transducer was analyzed by LabVIEW program. The results of the measurements for our transducer and LEM are shown in Figure 5.4 and 5.6, respectively. The noise of the NI-DAQ card and 16 sensors is 2.94 $mA_{rms}/\sqrt{Hz}$ @ 1 Hz (Fig. 5.4). The separate noise of the DAQ card itself is 1.38 $mA_{rms}/\sqrt{Hz}$ @ 1 Hz (Fig. 5.5). Measured noise of LEM sensor is 45.71 $mA_{rms}/\sqrt{Hz}$ @ 1 Hz.

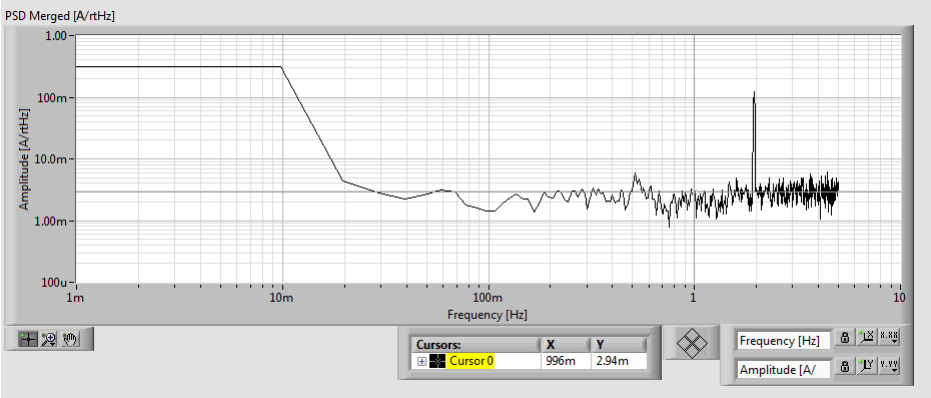

Figure 5.4: Measured noise of 16 sensors + NI-DAQ card

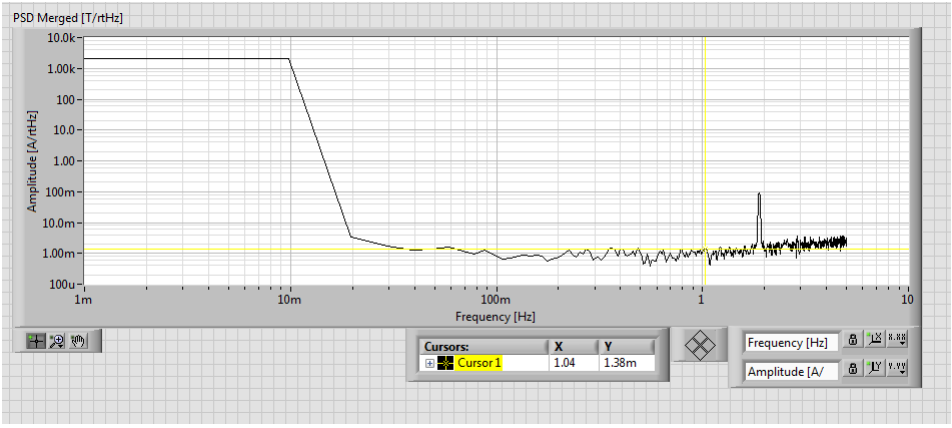

Figure 5.5: Measured noise of DAQ card itself

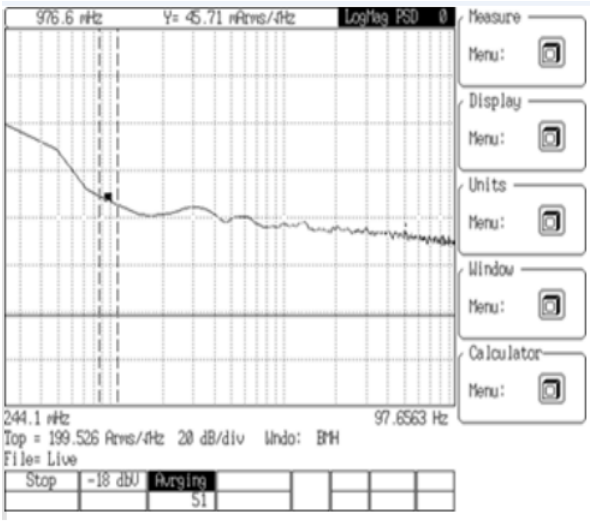

Figure 5.6: Measured noise of LEM sensor by SR770

5.3 Crosstalk error

The measurement error caused by a current in parallel to the current of interest is often referred to as crosstalk or crosstalk error [17, 18, 28, 29]. [30] presents the method for analytical crosstalk calculation for the circular array of microfluxgate TI DRV425 sensors.

The comparison of the crosstalk error for yokeless and LEM sensor is presented. Three different cases are examined (in-plane, 45°, and out-of-plane 10 A DC current). The crosstalk error for in-plane external current (0°) is shown in Figure 5.7, the same weights method has the error below 0.5% for 5 cm external current distance, LEM sensor has the error slightly below 1%. For 45° external current the crosstalk error is same low as shown in Figure 5.8, and depends on the position of the Hall sensor inside the magnetic yoke (core is asymmetric). The crosstalk error for yokeless sensor in the case of

out-of-plane external current (90°) is much smaller than for LEM sensor as shown in Figure 5.9. But, generally, we can conclude that both transducers have similar crosstalk error.

The crosstalk error for the different number of operating sensors is shown in Figure 5.10. As was mentioned above, the higher number of the sensors provides us with the more precise current calculation and more immune measurement against the external disturbances. For the minimum distance, the reading error is 1% for 16 operating sensors and 5.8% for 8 operating sensors.

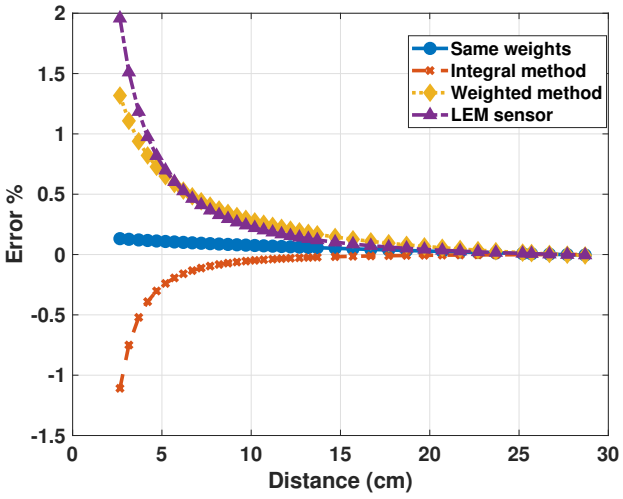

Figure 5.7: Measured crosstalk error for in-plane disturbance current

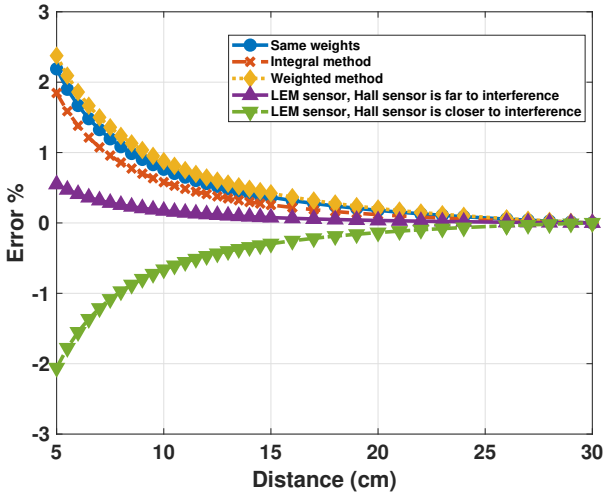

Figure 5.8: Measured crosstalk error for 45° disturbance current [8]

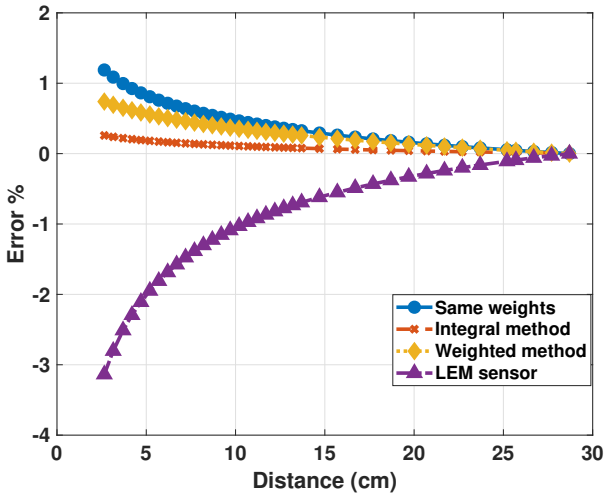

Figure 5.9: Measured crosstalk error for out-of-plane disturbance current [8]

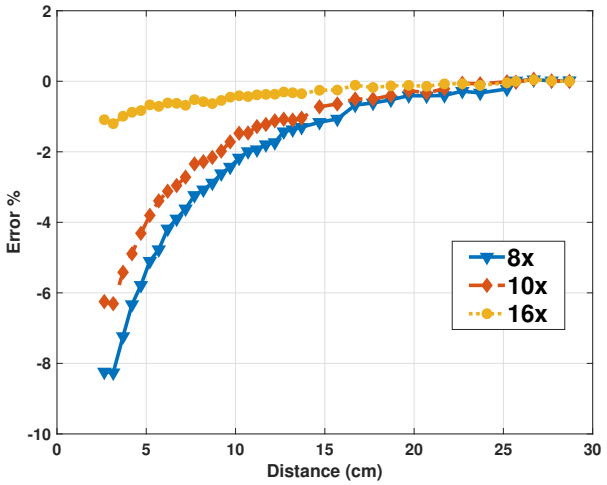

Figure 5.10: Reading error for different number of the operating sensors [8]

Chapter 6

Results

The novel method for the measurement of the currents in three-phase systems is presented in this thesis. The external disturbance cannot be canceled completely because the disturbance is not at the one point, i.e., the position and amplitude are unknown, and the DC component and field gradients up to 2^{nd} order are suppressed. With the increasing number of the operating sensor, the higher order of the field gradients can be suppressed, e.g., up to 4^{th} order for 8 sensors, and up to 6^{th} order for 10 sensors. The presented method suppresses the external disturbance from 70% reading error to 5% (14x times). The resolution of tens mA is achievable since the microfluxgate sensors have the small noise (6 $mA/\sqrt{Hz}$) @ 1 Hz with the full-scale 1000 A. If we compare our sensor with other commercially available sensors, e.g., mentioned above yokeless sensor SENIS BBM, our sensor has the smaller offset drift 8.5 mA/$°C$ in comparison with 75 mA/$°C$ SENIS BBM1000.

These results will be presented at *Magnetic frontiers 2019 Conference* in Lisbon, Portugal.

The rectangular current transducer has the range 400 A and was compared with the LEM HOP-800SB sensor. The rectangular transducer has a smaller size, 10x smaller noise, and temperature drift and the lower price. The results of the AC and DC measurement during 3 hours in Mírovka distribution station of the LEM and the rectangular transducer is shown in Figure 6.1 and 6.2, respectively. The temperature drift is observed from 9 AM to 10 AM on the LEM sensor due to the change in the ambient temperature, AC current is fully matched between two transducers.

This transducer was presented at the *IEEE Sensors* conference in Delhi, India.

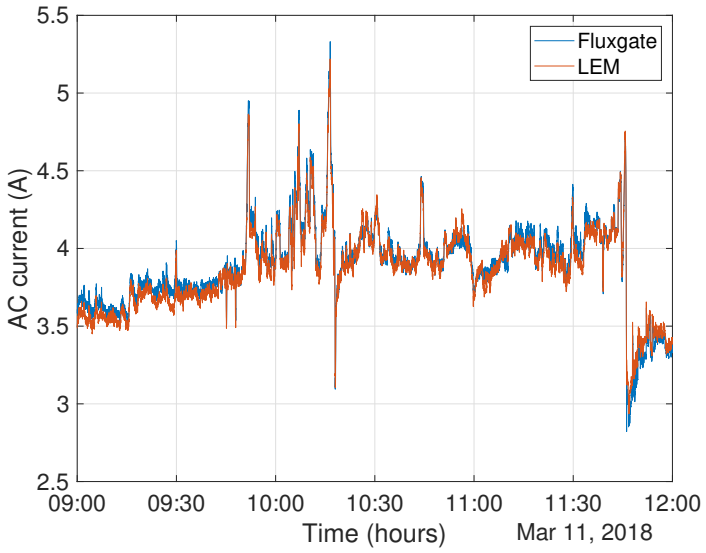

Figure 6.1: AC comparison of LEM and rectangular sensor

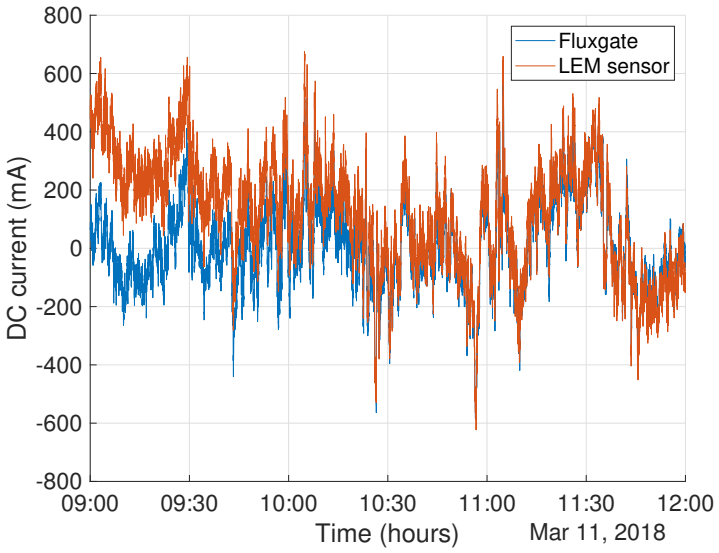

Figure 6.2: DC comparison of LEM and rectangular sensor

Chapter 7

Conclusion

- **Three-phase busbar current transducer**

  Three-phase AC/DC current sensors are required for smart grids. The three-phase current transducer is designed in this thesis. The method for the measurement of the three-phase currents with the suppression of the external fields and field gradients up to 2^{nd} order is provided. This solution has the compact size, high temperature stability (for DRV425 - offset drift is 5nT/°C corresponding to 8.5 mA/°C in described configuration), high current range up to 1000 A and even higher, low power consumption (less than 1 W for three transducers), linearity of 0.1%, and excellent immunity to external magnetic fields. The crosstalk error for external currents was reduced by the factor of 10 or more for the 240 mm distance to the external current, crosstalk between 3 phases for this configuration is eliminated completely. The FEM results are confirmed by the measurements, and maximum error between the experimental and simulation results is below 2%. The theoretical framework is invented for effective and fast computation on the microprocessors.

  The disadvantage of this solution is the frequency dependence, i.e., for each frequency sensor should be calibrated again, and the high dependence on the position inside the drilled hole in the busbar.

- **Rectangular array current transducer**

  This transducer has a high FS range up to 400 A but can be increased by the changed distance from the microfluxgate sensors to the conductor. This sensor is compared with the commercial standard, and the main advantages of this sensor are 10x lower noise, 10x lower temperature drift, more compact size, lower price, and same low crosstalk error.

  The disadvantage of this type of the transducer is more complex signal processing (16 analog signals from the sensors), the dependence on the position of the conductor inside the transducer, and dependence on the permeability of the conductor.

  Currently, this sensor is installed on the neutral line in Mírovka distribution station in the Czech Republic for long-term measurement of the geomagnetically induced currents (Figure 7.1).

Figure 7.1: Installed rectangular and LEM current sensor on the neutral line in Mírovka distribution station

Bibliography

[1] Atimex company. Catalog: Shunt 2000a/50mv-0,5 / 3xm10. *Official Web Page*.

[2] IndiaMART company. Catalog, CT current transformers, ring core type CT. *Official Web Page*.

[3] MECO company. Catalog: Clamp-on CT's and flexible AC current probe. *Official Web Page*.

[4] Pavel Kejik. *Contactless measurement of currents and current ratio by fluxgate method*. PhD thesis, Czech Technical University in Prague, 1999.

[5] Carolyn Mathas. The basics of current sensors. *Digikey - ArticleLibrary*, 2012.

[6] Pavel Ripka. *Magnetic sensors and Magnetometers*. Boston: Artech House, 2001.

[7] Texas Instruments. DRV425 fluxgate magnetic-field sensor. 2015.

[8] Andrey Chirtsov, Pavel Ripka, and Jan Vyhnanek. Rectangular array current transducer with integrated microfluxgate sensors. In *2018 IEEE SENSORS*. IEEE, oct 2018.

[9] Pavel Ripka. Electric current sensors: a review. *Measurement Science and Technology*, 21(11):112001, sep 2010.

[10] F. Koga, T. Tadatsu, J. Inoue, and I. Sasada. A new type of current sensor based on inverse magnetostriction for large current detection. *IEEE Transactions on Magnetics*, 45(10):4506–4509, oct 2009.

[11] Pavel Ripka, Karel Draxler, and Renata Styblikova. AC/DC current transformer with single winding. *IEEE Transactions on Magnetics*, 50(4):1–4, apr 2014.

[12] Xiaoguang Yang, Yuanyuan Li, Weidong Zheng, Wei Guo, Youhua Wang, and Rongge Yan. Design and realization of a novel compact fluxgate current sensor. *IEEE Transactions on Magnetics*, 51(3):1–4, mar 2015.

[13] Andrea Ajbl, Marc Pastre, and Maher Kayal. A fully integrated hall sensor microsystem for contactless current measurement. *IEEE Sensors Journal*, 13(6):2271–2278, jun 2013.

[14] Yuan-Pin Tsai, Kun-Long Chen, Yan-Ru Chen, and Nanming Chen. Multifunctional coreless hall-effect current transformer for the protection and measurement of power systems. *IEEE Transactions on Instrumentation and Measurement*, 63(3):557–565, mar 2014.

[15] Senis company. Catalog: Bus bar module current sensors bbm-01. *Official Web Page*.

[16] Zhang Zhenhong, Okabe Syuji, Akiyama Osamu, and Konno Hideto. Development of the highly precise magnetic current sensor module of +- 300 a utilizing amr element with bias-magnet. *IEEE Transactions on Magnetics*, 51(1):1–5, jan 2015.

[17] L. Di Rienzo and Z. Zhang. Spatial harmonic expansion for use with magnetic sensor arrays. *IEEE Transactions on Magnetics*, 46(1):53–58, jan 2010.

[18] L. Di Rienzo, R. Bazzocchi, and A. Manara. Circular arrays of magnetic sensors for current measurement. *IEEE Transactions on Instrumentation and Measurement*, 50(5):1093–1096, 2001.

[19] Pavel Mlejnek, Michal Vopálenský, and Pavel Ripka. AMR current measurement device. *Sensors and Actuators A: Physical*, 141(2):649–653, feb 2008.

[20] Pavel Ripka, Vaclav Grim, and Vojtech Petrucha. A busbar current sensor with frequency compensation. *IEEE Transactions on Magnetics*, 53(4):1–5, apr 2017.

[21] Pavel Ripka, Michal Pribil, Vojtech Petrucha, Vaclav Grim, and Karel Draxler. A fluxgate current sensor with an amphitheater busbar. *IEEE Transactions on Magnetics*, 52(7):1–4, jul 2016.

[22] Andrea Bernieri, Luigi Ferrigno, Marco Laracca, and Antonio Rasile. An AMR-based three-phase current sensor for smart grid applications. *IEEE Sensors Journal*, 17(23):7704–7712, dec 2017.

[23] Pavel Ripka, Václav Grim, and Andrey Chirtsov. Improved 3-phase current transducer. *Proceedings*, 2(13):1070, nov 2018.

[24] J.C. Olivares-Galvan, I. Hernandez, P.S. Georgilakis, and L.E. Campero. Calculation of the magnetic field intensity in a rectangular conductor carrying current in electromagnetism introductory courses. *Proceedings of the COMSOL Conference 2009 Boston*, 2009.

[25] Frank A. Benson. Skin effect (electricity). *AccessScience*, 2014.

[26] M. Mirzaei, P. Ripka, A. Chirtsov, P. Kaspar, and J. Vyhnanek. The effect of conductor permeability on electric current transducers. *AIP Advances*, 8(4):047506, apr 2018.

[27] L. Di Rienzo, R. Bazzocchi, and A. Manara. Circular arrays of magnetic sensors for current measurement. *IEEE Transactions on Instrumentation and Measurement*, 50(5):1093–1096, 2001.

[28] R Bazzocchi and L Di Rienzo. Interference rejection algorithm for current measurement using magnetic sensor arrays. *Sensors and Actuators A: Physical*, 85(1-3):38–41, aug 2000.

[29] Dongwei Li and Luca Di Rienzo. Robustness analysis of magnetic sensor arrays for current sensing. *2011 1st International Conference on Electric Power Equipment - Switching Technology*, oct 2011.

[30] Roland Weiss, Rory Makuch, Alexander Itzke, and Robert Weigel. Crosstalk in circular arrays of magnetic sensors for current measurement. *IEEE Transactions on Industrial Electronics*, 64(6):4903–4909, jun 2017.

Appendix A

Appendix

Content on the CD

1. Master thesis in PDF
2. Program in LabVIEW with the user manual
3. Matlab script for analytical computation
4. ANSYS 3D model
5. Pavel Ripka, Michal Přibil, Vojtěch Petrucha, Václav Grim, and Karel Draxler. *A Fluxgate Current Sensor With an Amphitheater Busbar*. IEEE TRANSACTIONS ON MAGNETICS, VOL. 52, NO. 7, JULY 2016
6. Pavel Ripka, Václav Grim, and Vojtěch Petrucha. *A Busbar Current Sensor With Frequency Compensation*. IEEE TRANSACTIONS ON MAGNETICS, VOL. 53, NO. 4, APRIL 2017
7. Andrey Chirtsov, Pavel Ripka, Jan Vyhnánek. *Rectangulararray current transducer with integrated microfluxgate sensors*, In: Proceeding - 2018 IEEE SENSORS. IEEE SENSORS, 2018..

A Fluxgate Current Sensor With an Amphitheater Busbar

Pavel Ripka[1], Michal Přibil[1], Vojtěch Petrucha[1], Václav Grim[1], and Karel Draxler[1,2]

[1]Czech Technical University, Prague 166 36, Czech Republic
[2]Czech Metrology Institute, Prague 150 72, Czech Republic

Large dc and ac electric currents are often measured by open-loop sensors without a magnetic yoke. A widely used configuration uses a differential magnetic sensor inserted into a hole in a flat busbar. The use of a differential sensor offers the advantage of partial suppression of fields coming from external currents. Hall sensors and AMR sensors are currently used in this application. In this paper, we present a current sensor of this type that uses novel integrated fluxgate sensors, which offer a greater range than magnetoresistors and better stability than Hall sensors. The frequency response of this type of current sensor is limited due to the eddy currents in the solid busbar. We present a novel amphitheater geometry of the hole in the busbar of the sensor, which reduces the frequency dependence from 15% error at 1 kHz to 9%.

***Index Terms*— Busbar sensor, current sensors, integrated fluxgate, microfluxgate.**

I. Introduction

LARGE dc and ac electric currents are often measured by open-loop sensors without a magnetic yoke [1]. The reason is that the yoke becomes bulky for uncompensated large current sensors, and fluxgate-based compensated sensors are rather complicated and energy-consuming [2], [3]. Introducing gaps into the magnetic yoke reduces the yoke size without saturation, but the gaps reduce the immunity of the core against the external fields [4].

Commercially available yokeless current sensors, such as Senis BBM [5], use Hall sensors on both the sides of the bus bar. The advantage of using a differential configuration is the partial suppression of the external magnetic fields, including those coming from currents in other conductors. The disadvantage is the large linearity error (typically 1.5%), poor offset stability, and high temperature coefficient of sensitivity. The available measurement ranges are typically 100–3000 A.

Another configuration, which is also used in this paper, has a differential magnetic sensor inserted into the hole in a flat busbar. Hall sensors and Anisotropic MagnetoResistive (AMR) sensors are currently used in this application. A 300 A AMR sensor with 0.5% linearity error was reported in [6].

It is well known that the precision of busbar current sensors for ac measurements is seriously limited due to the non-uniform current distribution caused by eddy currents in the solid bar. Attempts to break the eddy currents by using a busbar made of insulated conductive sheets led to gross errors caused by the unpredictable non-uniform current distribution between the individual sheets. However, the frequency dependence of busbar sensors is usually not mentioned in the literature. Other types of current sensors have a much wider bandwidth, but they are bulky and expensive devices.

In this paper, we present a 1000 A busbar current sensor using novel integrated fluxgate sensors developed by Texas Instruments (TI) [7]. We mainly discuss the linearity and frequency characteristics that have been achieved. We show that these characteristics can be improved by using more a complicated hole shape than a simple cylinder.

Manuscript received November 6, 2015; revised February 2, 2016; accepted February 4, 2016. Date of publication March 9, 2016; date of current version June 22, 2016. Corresponding author: P. Ripka (e-mail: ripka@fel.cvut.cz).

Color versions of one or more of the figures in this paper are available online at http://ieeexplore.ieee.org.

Digital Object Identifier 10.1109/TMAG.2016.2540523

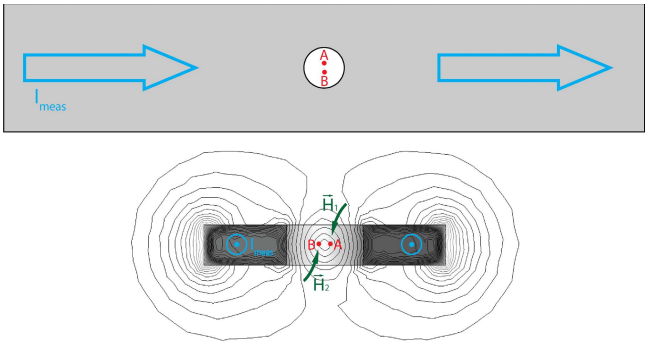

Fig. 1. Busbar current sensor with differential fluxgate sensors A and B at a distance $d = 2.5$ mm. (a) Top view. (b) Cross section.

The DRV425 TI integrated fluxgate sensor is a feedback-compensated sensor with on-chip excitation and signal processing circuits [8], [9]. The advantage of this sensor is its high excitation frequency, which gives a wide bandwidth of 47 kHz, a small sensor size of 4 mm × 4 mm, and a wide range of ±2 mT, whereas only ±100 μT range could be achieved with previous microfluxgate designs, which were restricted by the technological limitations of the CMOS design [10].

II. Simple Busbar Sensor With a Cylindrical Hole

The 300 mm × 60 mm × 10 mm copper busbar has a cylindrical hole of 19 mm in diameter with two fluxgates in locations A and B (Fig. 1), which measure the vertical component of the magnetic field. The sensors are connected to measure the field difference, which depends on the measured current. The gradiometer configuration suppresses common-mode magnetic fields such as the earth's field and the field from distant conductors. The field from conductors located nearby is only partially suppressed [11].

The sensor was tested at the accredited laboratory of the Czech Metrology Institute. The sensor linearity in the current range of 1000 A was better than 0.1% (Fig. 2). In fact,

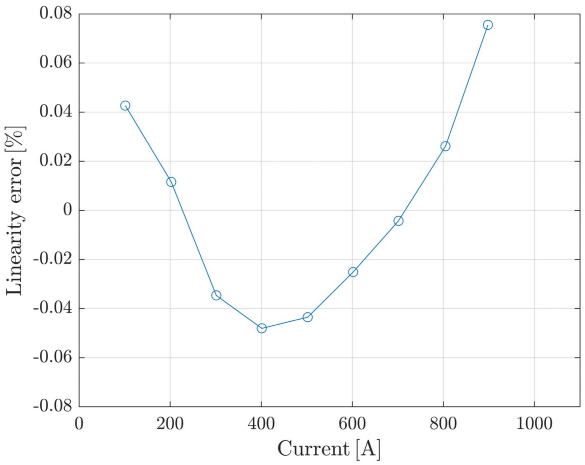

Fig. 2. Linearity error of the busbar current sensor from Fig. 1.

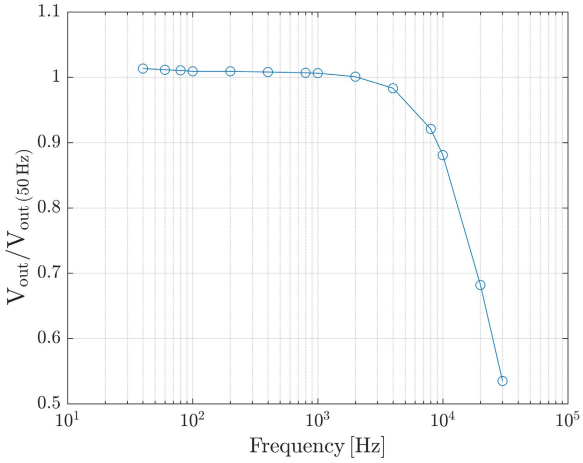

Fig. 3. Frequency characteristics of the integrated fluxgate.

even this non-linearity was caused by the metal objects in the laboratory. Due to the circular shape of the hole, the current lines in the vicinity of the sensor are also circular. The sensor constant is, therefore, very insensitive to the angular misalignment of the fluxgate.

The frequency characteristic of the integrated fluxgate was measured in ten-turn Helmholtz coils (Fig. 3). For each frequency step, the calibration field was calculated from the coil current. The calibration coil has negligible parasitic capacitance, which is demonstrated by its >1 MHz resonance frequency.

The measured characteristics show that up to 1 kHz, the frequency deviation of the bare fluxgate sensor is below 0.2%.

The frequency characteristic of the complete busbar current sensor is shown in Fig. 4. It is clear that the 15% frequency error at 1 kHz is caused by the busbar, not by the fluxgate sensor. This error is caused by the eddy currents in the busbar, which deflect the measured current toward the surface of the busbar and especially toward its edges. Some current lines are deflected toward the inner surface of the hole, i.e., closer to the sensor, but on an average, most of the current lines are

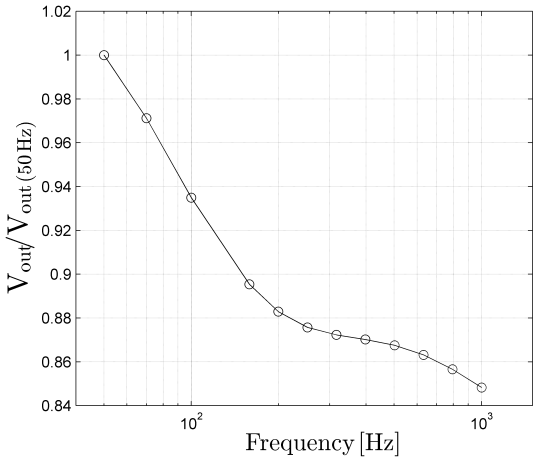

Fig. 4. Frequency characteristics of the busbar current sensor from Fig. 1. The error at 1 kHz is 14%.

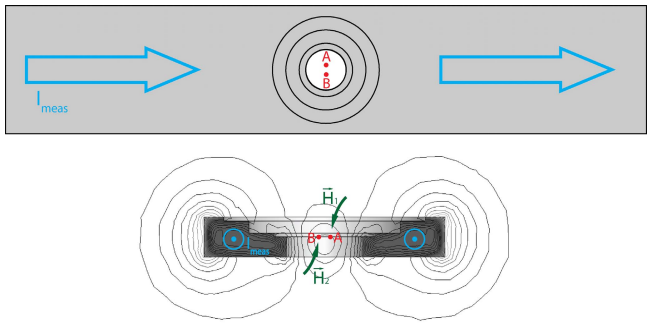

Fig. 5. Amphitheater current sensor—sensors are in central vertical position.

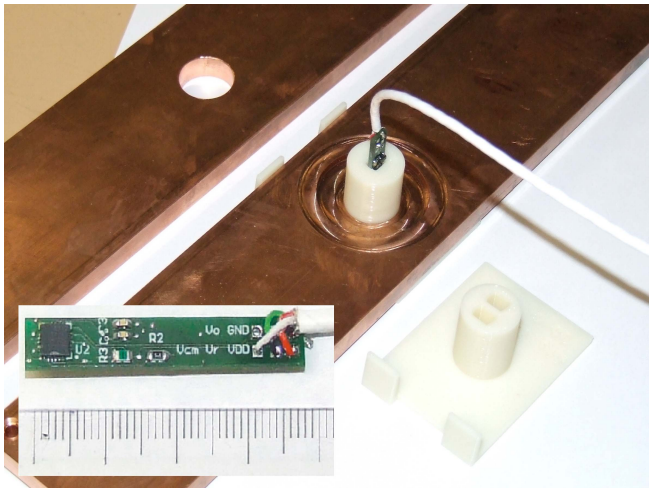

Fig. 6. Basic busbar sensor and amphitheater busbar current sensor with two sensors in the holder. Inset: Printed-circuit board (PCB) with fluxgate sensor.

deflected from the sensor. This causes a frequency-dependent drop in sensitivity.

III. Amphitheater Busbar Current Sensor

After a series of Finite-Element Method (FEM) simulations, we proposed the amphitheater shape of the busbar, as shown in Fig. 5, together with the location of the fluxgate sensors and the magnetic field lines. Fig. 6 shows the prototypes of both

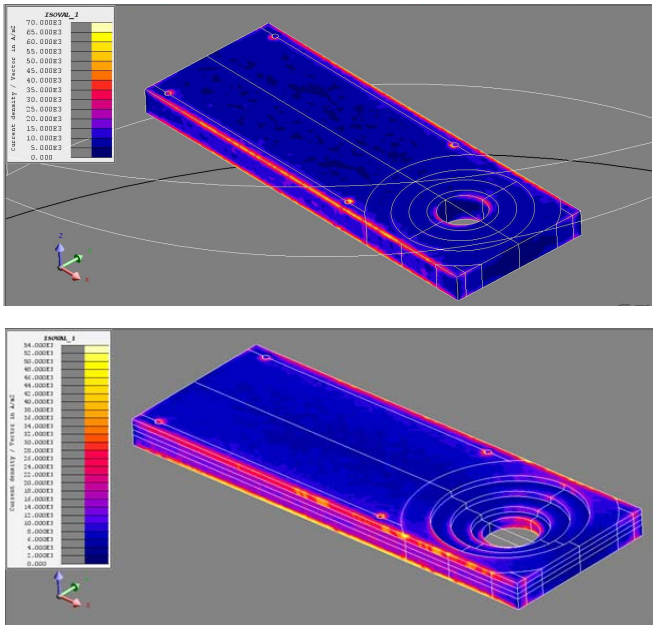

Fig. 7. FEM simulation of the ac current distribution in the busbar sensor and in the amphitheater current sensor.

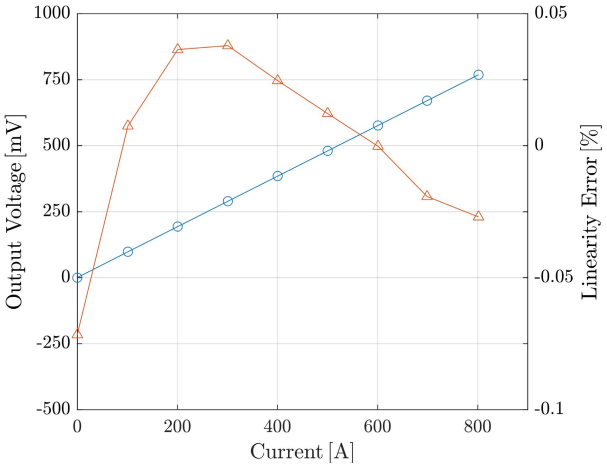

Fig. 8. Transfer function (straight line with circles) and linearity error (triangles) of the amphitheater current sensor (central sensor position).

the busbars: with a cylindrical hole and with an amphitheather hole. The fluxgate sensors are inserted into the slot in the plastic holder, which keeps them in a desired fixed position inside the busbar hole.

Fig. 7 shows an FEM model of the ac current distribution in the amphitheather busbar. The increased field density at the edges is clearly visible. This was the basic intuitive idea behind using this shape: the larger number of corners and the larger surface closer to the sensor deflect the current distribution to partly compensate the sensitivity frequency dependence.

Fig. 8 shows that the linearity of the novel sensor is not compromised: the linearity error is well below 0.1% for currents up to 800 A. The sensitivity to the current depends on the vertical position of the fluxgate sensor in the hole (Fig. 9). The maximum sensitivity point is not in the central plane,

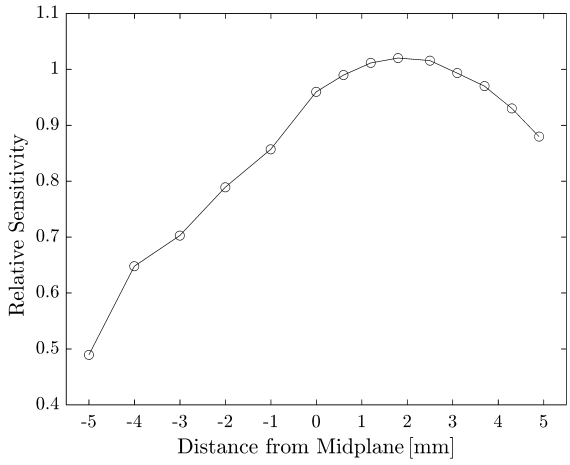

Fig. 9. Relative sensitivity as a function of the vertical sensor position for the amphitheater sensor.

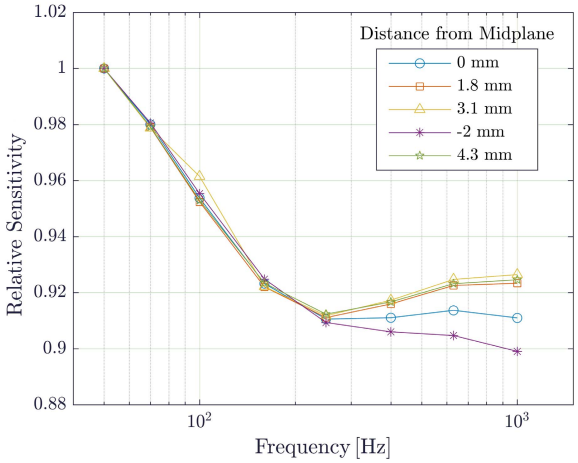

Fig. 10. Frequency characteristics of the amphitheater current sensor as a function of the sensor vertical position. The maximum error caused by the frequency characteristic was reduced to 9%.

as in the case of a simple busbar sensor, but 2 mm above the central plane. At this location, the sensitivity to position error is also minimized. This is a critical property, as with changing temperature due to self-heating the geometry changes due to thermal dilatations, and the current sensor needs to be robust against these changes.

The frequency characteristic of the amphitheater current sensor also changes as a function of the vertical position of the fluxgate. The dependence is shown in Fig. 10. Again, the characteristic is very stable in the vicinity of the previously determined working point 2 mm above the midplane. The maximum error caused by the frequency characteristic was reduced to 9%.

We also tested the current sensor performance for different spacing of the fluxgate. When the spacing is increased, the sensitivity increases, but the full-scale range decreases. This property is regularly used to set the current sensor range. We verified that changing the sensor distance has no major influence on the frequency characteristic, as shown in Fig. 11.

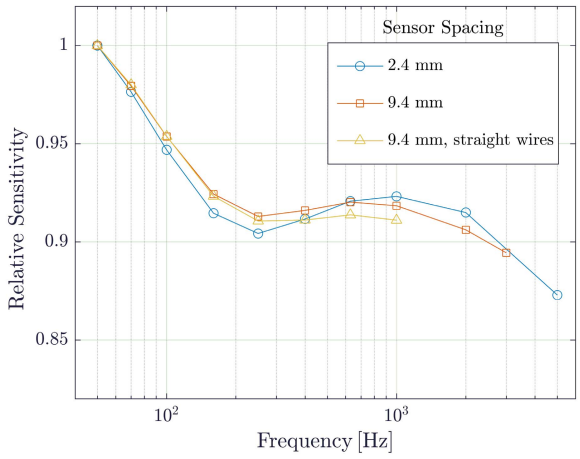

Fig. 11. Frequency characteristic of the amphitheater current sensor as a function of sensor spacing.

IV. Conclusion

Using integrated fluxgate sensors, we have designed a 1000 A current bar sensor with 0.1% linearity. The novel shape of the hole in the current bar reduces its frequency dependence from 15% error at 1 kHz to 9%.

Acknowledgment

This work was supported in part by Texas Instruments and in part by the Grant Agency of the Czech Republic under Grant P102/12/2177.

References

[1] P. Ripka, "Electric current sensors: A review," *Meas. Sci. Technol.*, vol. 21, no. 11, pp. 1–23, 2010.

[2] G. Velasco-Quesada, M. Roman-Lumbreras, A. Conesa-Roca, and F. Jeréz, "Design of a low-consumption fluxgate transducer for high-current measurement applications," *IEEE Sensors J.*, vol. 11, no. 2, pp. 280–287, Feb. 2011.

[3] X. Yang, Y. Li, W. Zheng, W. Guo, Y. Wang, and R. Yan, "Design and realization of a novel compact fluxgate current sensor," *IEEE Trans. Magn.*, vol. 51, no. 3, Mar. 2015, Art. no. 4002804.

[4] F. Koga, T. Tadatsu, J. Inoue, and I. Sasada, "A new type of current sensor based on inverse magnetostriction for large current detection," *IEEE Trans. Magn.*, vol. 45, no. 10, pp. 4506–4509, Oct. 2009.

[5] *Current Sensors BBM Manufactured by Senis, Catalogue*, accessed on Apr. 30, 2016. [Online]. Available: http://www.senis.ch/

[6] Z. Zhenhong, O. Syuji, A. Osamu, and K. Hideto, "Development of the highly precise magnetic current sensor module of +/−300 A utilizing AMR element with bias-magnet," *IEEE Trans. Magn.*, vol. 51, no. 1, Jan. 2015, Art. no. 4000205.

[7] *DRV425 Fluxgate Magnetic-Field Sensor, Texas Instruments Datasheet*, accessed on Apr. 4, 2016. [Online]. Available: http://www.ti.com/product/DRV425/datasheet

[8] M. Kashmiri, W. Kindt, F. Witte, R. Kearey, and D. Carbonell, "A 200 kS/s 13.5 b integrated-fluxgate differential-magnetic-to-digital converter with an oversampling compensation loop for contactless current sensing," in *Proc. IEEE Int. Solid-State Circuits Conf.*, Feb. 2015, pp. 1–3.

[9] M. F. Snoeij, V. Schaffer, S. Udayashankar, and M. V. Ivanov, "An integrated fluxgate magnetometer for use in closed-loop/open-loop isolated current sensing," in *Proc. ESSDERC/ESSCIRC*, Sep. 2015, pp. 263–266, paper 1014.

[10] P. M. Drljaca, P. Kejik, F. Vincent, D. Piguet, and R. S. Popovic, "Low-power 2-D fully integrated CMOS fluxgate magnetometer," *IEEE Sensors J.*, vol. 5, no. 5, pp. 909–915, Oct. 2005.

[11] P. Ripka, P. Kašpar, and J. Saneistr, "Geometrical selectivity of current sensors," *Przeglad elektrotechniczny*, vol. 88, no. 5a, pp. 38–39, 2012.

A Busbar Current Sensor With Frequency Compensation

Pavel Ripka, Václav Grim, and Vojtěch Petrucha

Faculty of Electrical Engineering, Czech Technical University in Prague, 166 27 Praha, Czech Republic

DC/AC yokeless galvanically insulated electric current sensors are required for applications, e.g., in automotive and aerospace engineering, where size, weight, and/or price are strictly limited. A busbar current sensor with differential fluxgate in the hole has 1000 A range and 10 mA resolution. Using an asymmetric shape, we achieved a frequency error below ±3% up to 1 kHz, while keeping high temperature stability and low sensitivity to mechanical misalignments. The 2.5 mA/°C maximum dc drift is four times better than when using an AMR sensor and 1000 times better than when using a Hall sensor. The sensor linearity error is below 0.1%.

***Index Terms*— Current sensor, fluxgate, magnetic sensor.**

I. Introduction

COMPACT yokeless current sensors are small, lightweight, and cheap. They are used in mobile and embedded applications, and for measuring high dc/ac currents, for which a magnetic core would be too large [1]–[3].

A. Busbar Sensor With Magnetic Sensors on the Surface

Conventional busbar sensors use a pair of Hall sensors on the conductor surface [4], [5]. Differential configuration partly suppresses the external fields. A current range of 10 kA is easily achievable [6], but the sensor has high offset drift. A current sensor based on magnetostriction has a similar problem with stability [7]. The use of an integrated fluxgate allows us to increase the range of the sensor to 600 A with a similar offset stability and noise. A disadvantage of current sensors of this type is their high sensitivity to the distance between the sensor and the conductor surface, which changes due to temperature dilatation. Our experiments have shown that a 0.1 mm shift of the sensor causes a 2% change in sensitivity. Another disadvantage of this type of current sensor is its very high frequency dependence: for a magnetic sensor directly on the surface of the busbar, the sensitivity at 1 kHz drops to 12% of the dc sensitivity.

B. Busbar Sensor With Magnetic Sensors in the Hole

A dc/ac current sensor with a differential integrated fluxgate inside the busbar is described in [8]. An advantage of this solution is that the range can easily be adjusted by changing the distance of the sensor from the busbar center, where the sensitivity is zero.

A similar busbar sensor with a range of 300 A is described in [9]. It uses an AMR sensor bridge in a semi-cylindrical slot in the busbar. Unlike the sensor described in [9], we use a differential sensor, which suppresses the influence of external currents and magnetic fields much more effectively.

Manuscript received August 9, 2016; revised October 18, 2016; accepted October 20, 2016. Date of publication October 25, 2016; date of current version March 16, 2017. Corresponding author: P. Ripka (e-mail: ripka@fel.cvut.cz).

Color versions of one or more of the figures in this paper are available online at http://ieeexplore.ieee.org.

Digital Object Identifier 10.1109/TMAG.2016.2620959

The busbar sensor with a hole has the advantage over a sensor on the surface that the frequency dependence is lower. With a cylindrical hole, the frequency error is 14%, while for amphitheater geometry, the error was reduced to 9% [10]. Problems with amphitheater geometry were the large sensitivity to a geometrical mismatch, and increased manufacturing complexity.

This paper presents the new shape of the busbar and the optimization of the sensor position, which led to ±3% frequency error from dc to 1 kHz. Sensitivity to temperature dilatation and geometrical mismatch is also analyzed.

All electromagnetic field simulations were performed in Ansys Maxwell using a 3-D eddy current solver and adaptive meshing. The final solution uses approximately 600k tetrahedra. Effects of heating were examined by co-simulation between Maxwell 3-D (to calculate losses) and Ansys Mechanical (to get temperature distribution).

II. Sensor Design

A. Differential Fluxgate Sensor

For the current sensor, we use the integrated fluxgate DRV425, manufactured by Texas Instruments [11]. The main advantage of this sensor is its low offset drift with temperature 5 nT/°C compared with AMR (20 nT/°C) and the Hall sensor (5 μT/°C).

Two fluxgate sensors were connected in a differential mode. Each sensor is individually feedback compensated, and we process the difference between the compensation currents. All the necessary electronics is integrated inside the sensor chips. The only external components are the sensing resistors. The compensation current flowing through the microfabricated solenoid compensation coil is in the range of 10 mA for the measured current of 1000 A. This high ratio cannot be achieved by a fluxgate-based ac/dc current transformer, due to the high parasitic capacitance of the secondary winding [12].

The two fluxgate sensors are mounted on the opposite sides of the printed circuit board. The effective distance between the sensors was 2.7 mm.

B. Busbar Geometry

Fig. 1 shows the electric current distribution inside the 60 mm × 10 mm conductor and the magnetic field in the free air for a central cylindrical hole 19 mm in diameter. While

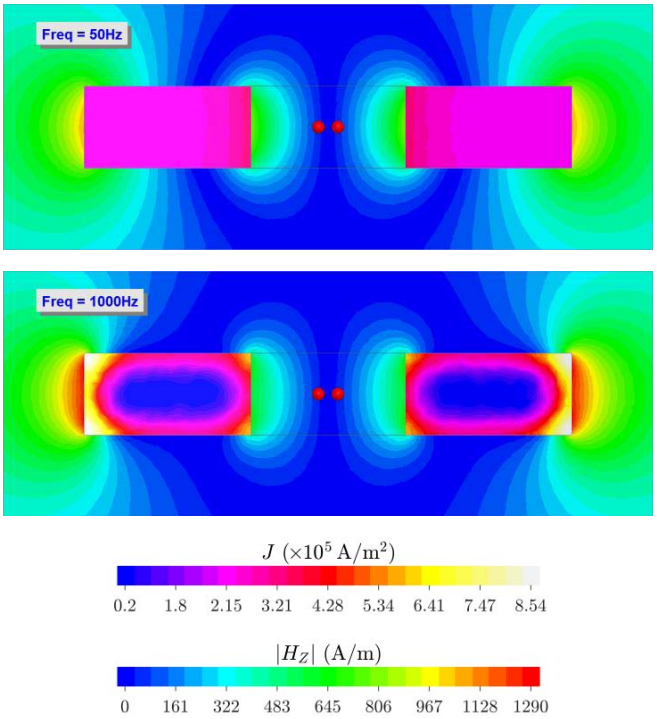

Fig. 1. Electric current distribution inside the 60 mm × 10 mm conductor and the magnetic field in the free air for a central cylindrical hole 19 mm in diameter. The FEM simulation was performed for $f = 50$ Hz and 1 kHz. Red dots: sensor positions.

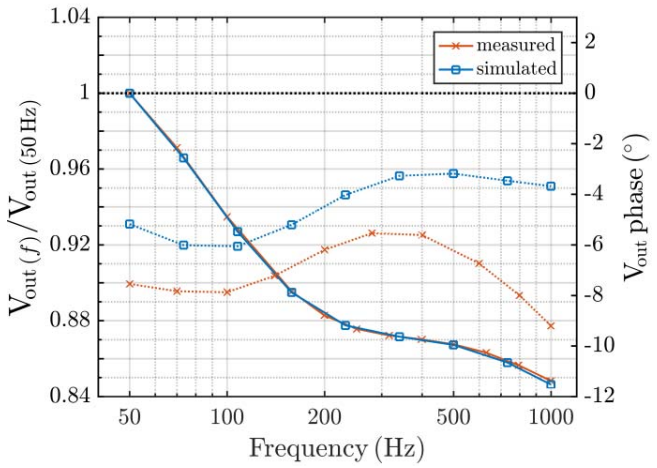

Fig. 2. Frequency dependence of the busbar current sensor with the traditional symmetrical design (measurement and 3-D simulation). Full line: amplitude characteristics. Dotted line: phase characteristics.

the current is very homogeneous for a frequency of 50 Hz, at 1 kHz, the effect of an eddy current increased the current density at the external corners by a factor of 1.5. As these regions are further away from the sensors, this results in a decreased sensitivity of the sensor.

The frequency dependence as a result of 3-D simulation and measurement is shown in Fig. 2 for a differential magnetic sensor having a gradiometric distance of 2.7 mm. The frequency error of 16% at 1 kHz should be compared with the 32% error of the transducer based on Hall sensors on the surface of the busbar [5]. The phase error at 1 kHz is 10°,

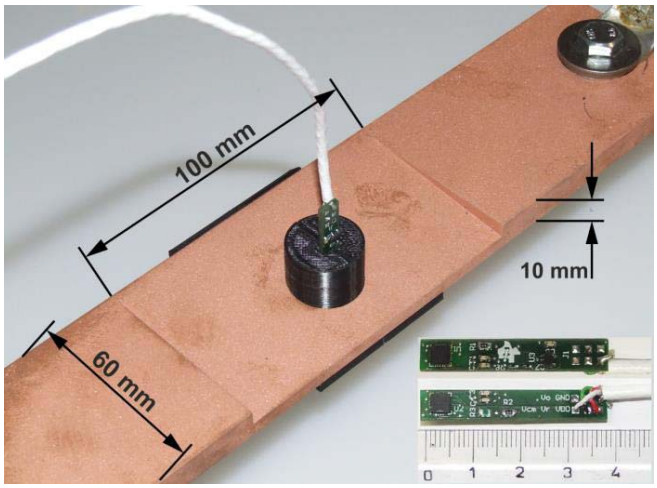

Fig. 3. New busbar sensor with a wedge-shaped profile. The circular hole is located asymmetrically and the position of the sensors in the hole is also asymmetrical.

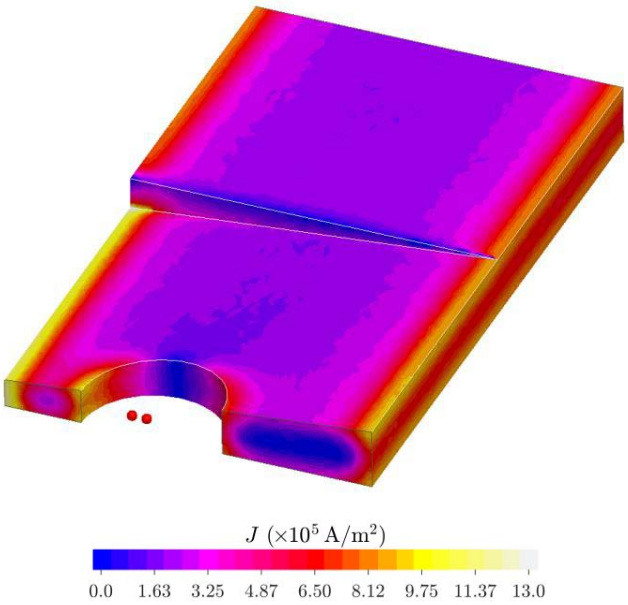

Fig. 4. Electric current distribution in the new busbar sensor at 1 kHz. Red dots: sensor positions.

which is too large for this sensor to be used for power and energy measurements. We attribute the difference between the simulated and measured phase characteristics to error in simulation, as we observed negligible phase error of the sensor itself at low frequencies.

In order to better compensate the frequency dependence, we analyzed a range of alternative geometries. Based on 3-D Finite-Element Modelling (FEM) simulations, we selected an asymmetric design with a wedge bar. The new sensor is shown in Fig. 3. The dimensions were selected, so that the sensitivity is approximately 1 mV/A. As the fluxgate sensitivity is 488 mV/mT (12.2 mA/mT with a 10 Ω sensing resistor and an instrumentation amplifier with gain of 4), the corresponding field factor is 500 A/mT.

Fig. 4 shows the 3-D FEM simulation of the current distribution of the new asymmetric design. Because of the

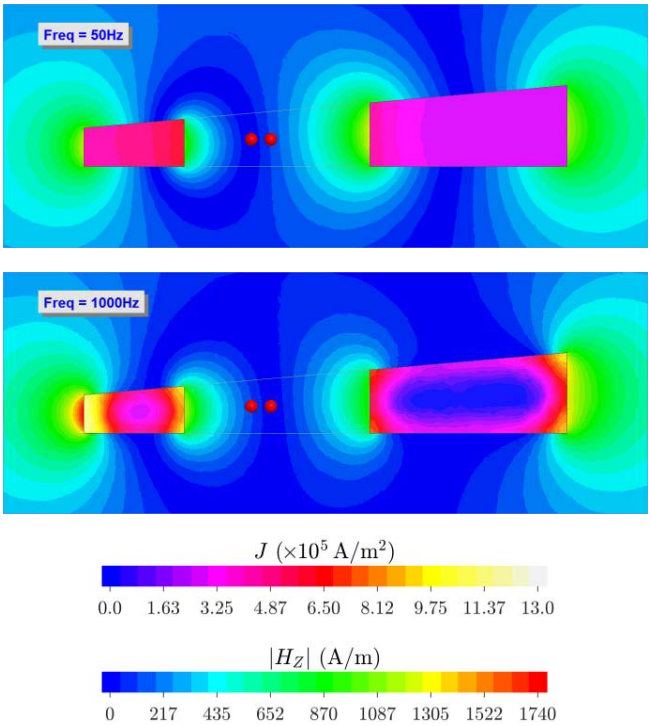

Fig. 5. Current and field distribution in the new busbar sensor with a wedge-shaped profile. 3-D FEM simulation at 50 Hz and 1 kHz. Red dots: sensor position.

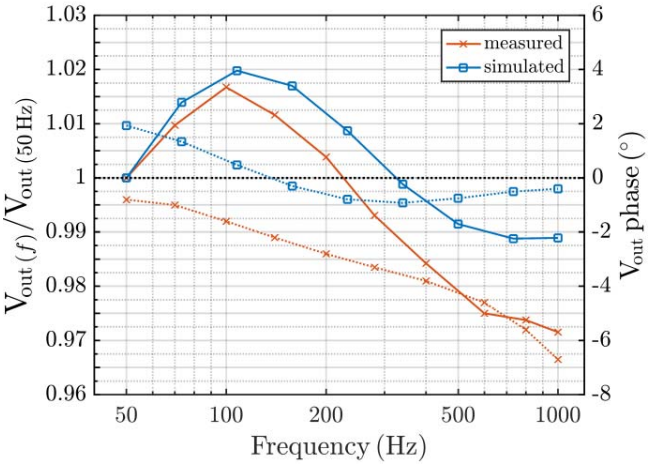

Fig. 6. Frequency dependence of the busbar current sensor with the new asymmetrical design (measurement and 3-D simulation). Full line: amplitude characteristics. Dotted line: phase characteristics.

modified shape, the current is even more redistributed due to the eddy currents. Fig. 5 shows the current and magnetic field distribution in the central plane, where both magnetic sensors are located. It is clear that the field gradient is more frequency dependent than the previous geometry. We solved the task of selecting the position of the differential sensor pair to minimize the frequency dependence while keeping a reasonable conversion factor and low sensitivity to misalignment. This optimization was made by parametric FEM simulation. The selected sensor locations are marked by red dots.

The measured frequency characteristics shown in Fig. 6 confirmed the expectations from the simulations. The measured

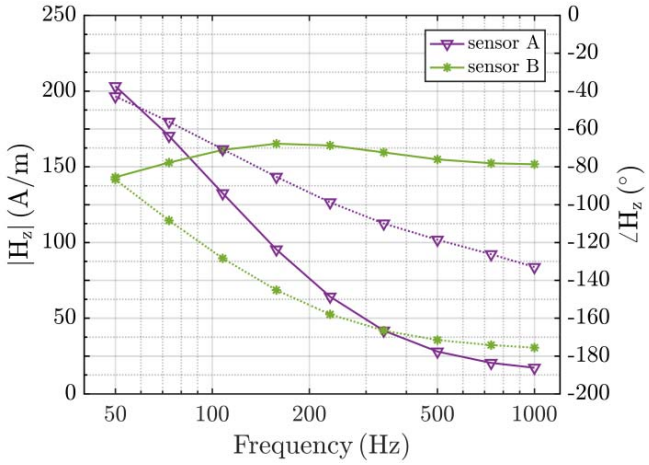

Fig. 7. Simulated frequency dependence of individual sensors.

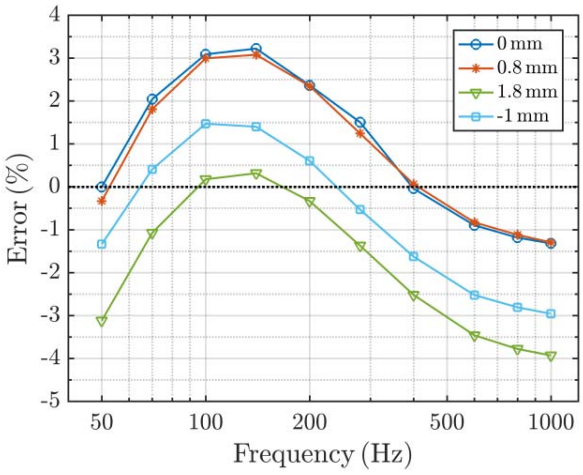

Fig. 8. Measured frequency characteristics for several values of the vertical position of the sensors in the hole. The graph shows deviation from sensitivity at 50 Hz.

frequency error up to 1 kHz is below 3%. The phase error was only slightly reduced to 8° at 1 kHz, but up to 600 Hz, the phase characteristics is linear.

Fig. 7 shows the principle of the compensation mechanism: the frequency dependence of the individual sensors is high. The differences are caused by different effect of eddy currents in each point. In this way, the frequency dependence of the differential signal is dramatically decreased. If we vectorially subtract voltages for A and B sensors, we obtain theoretical characteristics shown in Fig. 6.

The compensation technique based on the subtraction of two similar variables raises the question of the stability of this compensation in real conditions. We therefore studied the stability of the sensor with temperature and geometrical tolerances.

III. Sensor Stability and Resistance to External Currents

Fig. 8 shows how the frequency characteristics change with vertical sensor misalignment. It is clear that the changes in the shape of the frequency characteristics are negligible, but the

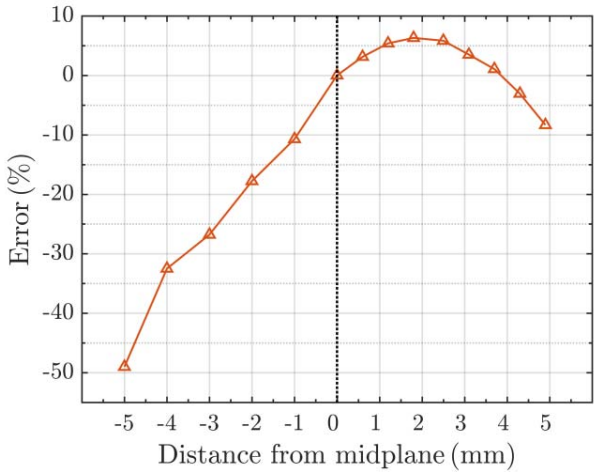

Fig. 9. Dependence of the sensitivity on the vertical position of the sensors in the hole. The graph shows deviation from sensitivity at the central point.

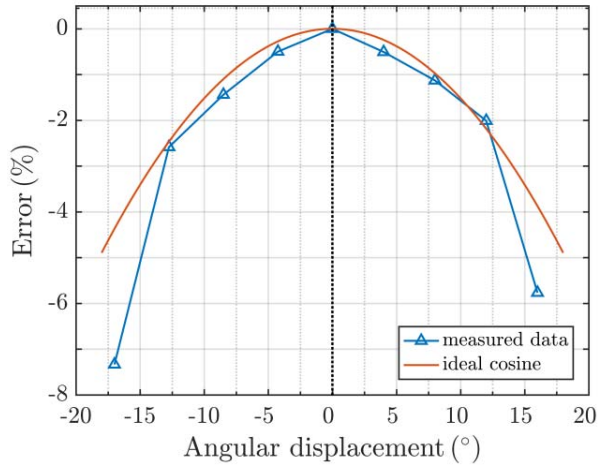

Fig. 10. Sensitivity error caused by rotational displacement of the sensor. The theoretical error caused by cosine dependence is shown for comparison.

sensitivity depends on the vertical position of the sensor, as shown in Fig. 9. The maximum sensitivity point is not in the central plane, as for a simple busbar sensor, but 2 mm above. In this optimum location, the sensitivity to position error is also minimized.

Fig. 10 shows the sensitivity to rotational displacement of the differential sensor. It is clear that the characteristics differ significantly from the cosine shape. By linear approximation, we may estimate that 0.2° angular displacement caused by temperature cycling would cause only 0.025% error, which is negligible in comparison with the 0.1% linearity error of the device.

We also examined the effect of self-heating by FEM simulations. At a maximum current of 1000 A, the temperature of the current bar is 50 °C. The sensitivity change caused by temperature effects is 1%. In comparison with this, the sensitivity change with the temperature of the fluxgate sensor itself is only 7 ppm/°C.

The dc offset stability depends mainly on the parameters of the fluxgate sensor. The specified maximum drift of 5 nT/°C would correspond to 2.5 mA/°C. The dc current resolution is limited to 10 mA, as the sensor noise power spectrum density is 2 mA/$\sqrt{\text{Hz}}$ at 1 Hz.

With a sensitivity of 500 A/mT, the calculated effect of an external 1000 A current at a distance of 15 cm is 3.4 μT, so the error is only 0.17%. We measured the influence of the external current in the real busbar and found a very similar error of 0.15%.

IV. Conclusion

The busbar fluxgate current sensor presented here has very small ferromagnetic cores inside the two integrated feedback-compensated fluxgate sensors. This keeps the power consumption of our device below 100 mW, even for the maximum measured current of 1000 A. This is much lower than the power consumption of around 15 W, even when using very efficient electronics, for another class of feedback-compensated fluxgate current sensors with large cores around the measured current conductor [13].

In addition to the advantages of the yokeless busbar current sensor, which are its small size, lightweight, and low power consumption, we also should mention its disadvantages. The sensor needs to be inserted into the measured circuit, which is not practical for ambulatory measurements. Compared with that, the yoke can be made openable as clamps. A yoke is also believed to better suppress the influence of external fields, but we have shown that the small distance of our differential sensor pair performs similarly, as the error for an external current at a distance of 15 cm is only 0.15%.

The new shape of the busbar sensor improved the frequency characteristics: the achieved error was ±3% in amplitude and 8° in phase at 1 kHz. The sensor linearity is 0.1%, in comparison with 1% in [9]. With 1000 A range, the sensor has 10 mA resolution and 2.5 mA/°C maximum dc drift. The temperature stability is, therefore, four times better than when using an AMR sensor and 1000 times better than when using Hall sensors. The external current in a 9 cm distant busbar is suppressed by a factor of 66.

Acknowledgment

The authors would like to thank A. Chirtsov, who performed some of the measurements. A. Chirtsov and V. Grim received student support from Texas Instruments, which also supplied the sensor boards.

References

[1] P. Ripka, "Electric current sensors: A review," *Meas. Sci. Technol.*, vol. 21, no. 11, pp. 1–23, Sep. 2010.
[2] G. Velasco-Quesada, M. Roman-Lumbreras, A. Conesa-Roca, and F. Jerez, "Design of a low-consumption fluxgate transducer for high-current measurement applications," *IEEE Sensors J.*, vol. 11, no. 2, pp. 280–287, Feb. 2011.
[3] X. Yang, Y. Li, W. Zheng, W. Guo, Y. Wang, and R. Yan, "Design and realization of a novel compact fluxgate current sensor," *IEEE Trans. Magn.*, vol. 51, no. 3, pp. 1–4, Mar. 2015.
[4] BBM. *Current Sensors Manufactured by Senis, Catalogue*, accessed Nov. 4, 2016. [Online]. Available: http://www.senis.ch/
[5] M. Blagojević, U. Jovanović, I. Jovanović, D. Mančić, and R. S. Popović, "Realization and optimization of bus bar current transducers based on Hall effect sensors," *Meas. Sci. Technol.*, vol. 27, no. 6, p. 065102, 2016.

[6] K.-L. Chen and N. Chen, "A new method for power current measurement using a coreless Hall effect current transformer," *IEEE Trans. Instrum. Meas.*, vol. 60, no. 1, pp. 158–169, Jan. 2011.

[7] F. Koga, T. Tadatsu, J. Inoue, and I. Sasada, "A new type of current sensor based on inverse magnetostriction for large current detection," *IEEE Trans. Magn.*, vol. 45, no. 10, pp. 4506–4509, Oct. 2009.

[8] M. F. Snoeij, V. Schaffer, S. Udayashankar, and M. V. Ivanov, "Integrated fluxgate magnetometer for use in isolated current sensing," *IEEE J. Solid-State Circuits*, vol. 51, no. 7, pp. 1684–1694, Jul. 2016.

[9] Z. Zhenhong, O. Syuji, A. Osamu, and K. Hideto, "Development of the highly precise magnetic current sensor module of $+/-300$ A utilizing AMR element with bias-magnet," *IEEE Trans. Magn.*, vol. 51, no. 1, pp. 1–5, Jan. 2015.

[10] P. Ripka, M. Přibil, V. Petrucha, V. Grim, and K. Draxler, "A Fluxgate Current Sensor With an Amphitheater Busbar," *IEEE Trans. Magn.*, vol. 52, no. 7, Jul. 2016, Art. no. 4002004.

[11] *DRV425 Fluxgate Magnetic-Field Sensor, Texas Instruments Datasheet*, accessed Nov. 4, 2016. [Online]. Available: http://www.ti.com/product/DRV425/datasheet

[12] P. Ripka, K. Draxler, and R. Styblikova, "AC/DC current transformer with single winding," *IEEE Trans. Magn.*, vol. 50, no. 4, Apr. 2014. Art. no. 8400504.

[13] G. Velasco-Quesada, M. Román-Lumbreras, R. Pérez-Delgado, and A. Conesa-Roca, "Class H power amplifier for power saving in fluxgate current transducers," *IEEE Sensors J.*, vol. 16, no. 8, pp. 2322–2330, Apr. 2016.

Rectangular array current transducer with integrated microfluxgate sensors

Andrey Chirtsov[1], Pavel Ripka[1], Jan Vyhnánek[1]
[1]Department of Measurement, Faculty of Electrical Engineering, Czech Technical University in Prague, Prague, Czech Republic
chirtand@fel.cvut.cz, ripka@fel.cvut.cz, vyhnajan@fel.cvut.cz

***Abstract*—Novel rectangular yokeless current transducer with the range 400 A using 16 microfluxgate sensors around the busbar conductor is presented in this paper. Compared to yokeless transducers utilizing the differential pair of magnetic sensors, our solution has much better suppression of external currents (lower crosstalk). Compared to industrial transducers with yoke, the new transducer has 10-times lower noise, 10-times better temperature stability, and same crosstalk. Sensor design, different methods for calculating the current and temperature dependence are presented in this paper. Crosstalk error is examined in dependence on the number of the operating sensors and external current position.**

Keywords—current sensor; microfluxgate sensors; rectangular sensor array, Finite element modelling;

I. INTRODUCTION

Contactless transducers that measure the electric current usually have a magnetic yoke around the current conductor. The purpose of the yoke is to concentrate the magnetic flux inside this yoke because of its small reluctance [1].

This method has definite advantages – the measurement does not depend on the position of the current conductor inside the yoke, and shields against the external magnetic fields. Hall sensors are dominant sensors that are used in connection with the magnetic yoke, but they can significantly affect the measurement accuracy such as temperature stability of the offset, gain, noise, and non-linear effects. The influence of these factors can be reduced by using a microsystem with continuous sensitivity calibration (achievable drift below 80 ppm/°C and nonlinearity is less than ± 0.08%) [2]. On the other hand, transducers with magnetic yoke has several disadvantages such as the size of the transducer since the sensor requires the sizable magnetic core, nonlinear effects of the magnetic material of the yoke due to the saturation and hysteresis of the core and the impossibility of using more precise magnetic sensors due to the concentrated magnetic field. Another approach for measuring current are the sensors without yoke. The first type of yokeless currents sensor uses hole drilled in the middle of the busbar with inserted 2 microfluxgate sensors located on opposite sides of the PCB [3]. This setup allows us to measure current with the range ±500A and with linearity error lower than 0.1%. The advantage of this solution is simplicity, low-power consumption and low-cost. The disadvantage of this method is mainly crosstalk effect which can be eliminated by using a configuration with 3x, 4x or 6x microfluxgate sensors [4] and need for the drilling hole in the middle of the busbar. The other problem is frequency dependence due to non-uniform current distribution caused by eddy currents in the solid bar. In [5] and [6] a busbar with an amphitheater hole and wedge bar respectively is shown, these methods significantly reduce frequency dependence. A similar busbar sensor with a range of 300 A is described in [7]. It uses an AMR sensor bridge in a semi-cylindrical slot in the busbar. Circular sensor array is also a common method of measurement providing less dependence of reading on the conductor position and better crossfield immunity [8]. This approach was recently used in [9] using microfluxgate sensors. The disadvantage of circular array is that the size of the transducer is impractical and makes its installation inaccessible in hard-to-reach places. Measuring setup with AMR sensors is also possible but this has insufficient range (±8A) due to the AMR sensor field range of 200 uT. [10].

II. YOKELESS CURRENT SENSOR DESIGN

In this paper, we suggest a new method for measuring the current flowing through the busbar without the yoke; instead the closed loop is approximated by 16 integrated microfluxgate sensors TI DRV425 placed on the circumference of the conductor. The sensor is designed for the maximum current of 400 A. Fluxgate sensors are much more sensitive than Hall sensors, and they have advantages over almost all characteristics such as temperature stability, noise and, non-linearity. The disadvantage is the relatively small full range with the comparison with Hall sensor which is 2 mT. The current transducer is designed to measure current in aluminum busbar conductor with the cross-section of 100x10 mm which is commonly used as the ground conductor in power stations as shown in Fig. 1. Using the current transducers on the iron introduce the additional errors and should be recalibrated due to the busbar permeability [11].

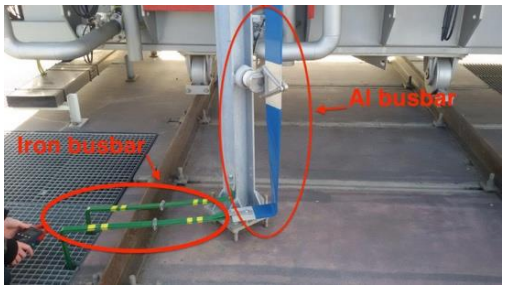

Figure 1: Al and Iron busbar as a ground conductor at the power station in the Czech Republic

The sensor has dimensions of 104x14 mm which makes it very compact and easy to install. Each microsensor is individually feedback compensated, and all necessary electronics is integrated inside the sensor chips, the only adjustable external

component is a shunt resistor. Full-scale (FS) range of the microsensor and, therefore, the current transducer can be adjusted using the shunt resistor. Utilizing such a number of operating sensors can significantly reduce the influence of the external magnetic fields including those caused by external currents by better approximation of the closed line integral in the Ampere's law. Finite element modeling is performed for design parameters of the sensor and the verification of the measurements. In further, FEM can be used to optimize the location and number of magnetic sensors to achieve desired precision and crosstalk error. The experimental model of the sensor is shown in Fig. 2. Commercially available LEM sensor HOP 800-SB is used to compare the properties of the yokeless current transducer. The LEM sensor consists of 2 Hall sensors, magnetic core and operates without feedback compensation. The distance between the particular integrated fluxgate sensors DRV425 is 14 mm, and the distance between the sensors and the surface of the busbar is 3.5 mm. Distribution of the microfluxgate sensors around the busbar is shown in Fig. 3. The sensor outputs are read by the NI-DAQ card and processed by the software.

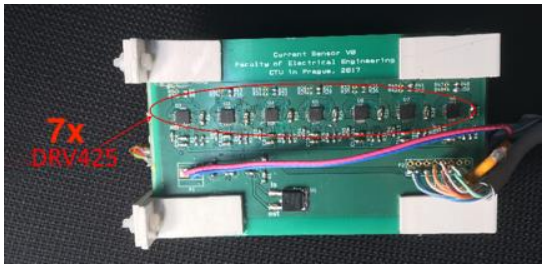

Figure 2: Picture of the yokeless current transducer with the 16 integrated microfluxgate sensors

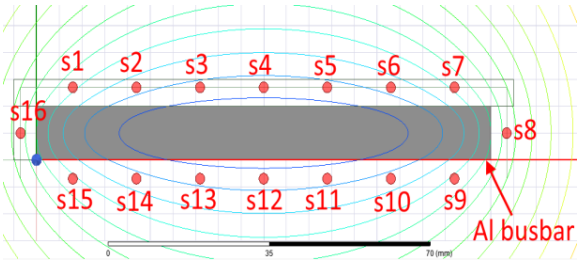

Figure 3: Distribution of the microfluxgate sensors around the busbar conductor

III. CALCULATING WEIGHTS COEFFICIENTS FOR EACH SENSOR

Each sensor should have individual weight for correct computation of the current. FEM simulation is performed to find the weights. For the material properties are the following parameters: for the aluminum relative permeability μ=1.000021 and conductivity S=31.713e^6 S/m. The electrical conductivity of the Al busbar was measured using 4 – terminal method with the measuring current of 50.25 A in the region of the homogenous current density. Three different methods of calculating the weight are used for each sensor. The sum of the sensor output signals is an approximation of the Ampere's magnetic field circulation.

A. Same weights

All particular sensors have the same weight w (A/ (A/m)). Current is calculated by (2). For DC current calculated weight is w_i = 0.0147, where w_i is the individual weight and H_i is the measured strength of the magnetic field for the i-th microfluxgate sensor. This method is the simplest one and does not require a lot of resources in the calculation of the current.

$$w = w_1 = w_2 = w_3 = \cdots = w_{16} \quad (1)$$

$$I_{measured} = w(H_1 + H_2 + H_3 + \cdots + H_{16}) \quad (2)$$

B. Integral method

The surface of the whole busbar is divided into separate regions corresponding to each of 16 sensors. These lines show the tangential component of the magnetic field strength at a distance of 3.5 mm from the edge of the busbar. For calculating the weights for each sensor, the line corresponding to the sensor is numerically integrated and divided by the theoretical value of the magnetic field strength obtained by FEM in the site of this sensor.

$$w_i = \frac{\int H_{t_i} dl}{H_{FEM}{}^i} \quad (3)$$

$$I_{measured} = (w_1 H_1 + w_2 H_2 + w_3 H_3 + \cdots + w_{16} H_{16}) \quad (4)$$

This coefficient should be calculated for each sensor separately, but these weights are symmetrical with respect to the center of the busbar. Total current is calculated by the (4).

C. Weighted method

The weight for each sensor was obtained by dividing the known applied current in simulation flowing the busbar by the theoretical value of the tangential magnetic field strength in the site of the sensor. The equation for calculating the weights for each sensor and the total current is shown in (5), (6), respectively.

$$w_i = \frac{I_{total_{simulation}}}{H_{FEMi}} \quad (5)$$

$$I_{measured=} = \frac{w_1 H_1 + w_2 H_2 + w_3 H_3 + \cdots + w_{16} H_{16}}{16} \quad (6)$$

IV. CHARACTERISTICS OF THE YOKELESS TRANSDUCER AND LEM SENSOR

A. Offset stability with temperature

Offset drift was tested only for three different temperatures. Results of the offset value for LEM and yokeless transducer for the various current calculation methods are shown in Table 1 and 2, respectively. The estimated values for the temperature drift are shown in Table 3.

TABLE I. MEASURED OFFSET VALUE AT DIFFERENT TEMPERATURES FOR LEM HOP 800-SB

Temperature (°C)	Offset (mA)
-22.2	2850
25.3	840
59.9	-1104.9

TABLE II. MEASURED OFSSET VALUES AT DIFFERENT TEMPERATURES FOR YOKELESS TRANSDUCER

Temperature (°C)	Offset (mA)		
	Same weights	Integral method	Weighted method
-11	-301	249	389
25.3	220	193	305
55	99	92.24	182.4

TABLE III. OFFSET TEMPERATURE DRIFTS CALCULATED FOR LEM AND YOKELESS TRANSDUCER

Parameters	LEM HOP 800-SB	Yokeless transducer		
		Same weights	Integral method	Weighted method
FS range	800	400		
Drift (mA/°C)	48.1	3.06	3.13	2.37
Drift (%FS/°C)	6e-3	7.65e-4	7.83e-4	5.93e-4

B. *Noise*

The noise analysis for LEM sensor is performed by FFT Analyzer SR770, and for the yokeless sensor the noise spectrum is calculated using the software. The measured power spectral density (PSD) for LEM sensor @ 1 Hz is 45.7 mArms/sqrt(Hz). For the yokeless sensor, the PSD is affected by two factors – the separate noise of the DAQ card and the sensors themselves. PSD of the DAQ card itself equals to 1.38 mArms/sqrt(Hz) @ 1 Hz, while total PSD (DAQ card + 16 sensors) is 2.94 mArms/sqrt(Hz) @ 1 Hz. We may conclude that the noise of yokeless transducer is much lower compared to the LEM HOP 800-SB.

C. *Crosstalk error of the reading*

External current has the significant influence on the current reading of both sensors. Response to the realistic external DC current 10 A in the perpendicular plane 90° and at 45° direction is measured and shown in Fig. 4 and 5, respectively. The main reason of the current reading error is the distance to the external current and the selected processing method for the yokeless current sensor, the dependence of the Hall sensors displacement of the LEM sensor due to the asymmetric split core. In the minimum realistic distance of 15 cm in power stations, the error of yokeless sensor is always below 0.5%, while for the LEM sensor the same error is 1%.

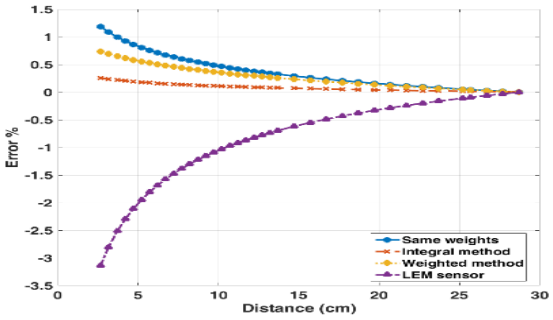

Figure 4: Reading error of the LEM and yokeless sensor: influence of the superior (90°) external DC current of 10 A as a function of the distance

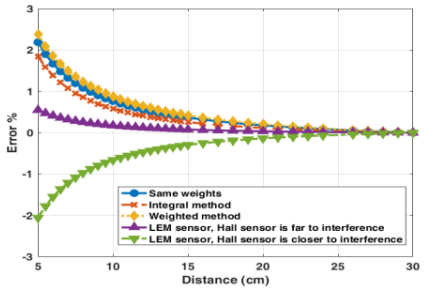

Figure 5: Reading error of the LEM and yokeless sensor: influence of the external DC current of 10 A as a function of the distance in 45° position

D. *Reading error in dependence on the operating sensors*

As mentioned above, the higher number of the integral points reduces the current reading error. Crosstalk error in dependence on the number of operating microsensors is shown in Fig. 6 for same weights method; for other methods this dependence is identical. The number of the sensors depends on the application as accurately and reliable the current should be measured. The current reading error is lowered since the larger number of the sensors allows us to better approximate the integral with an increase in the number of operating sensors.

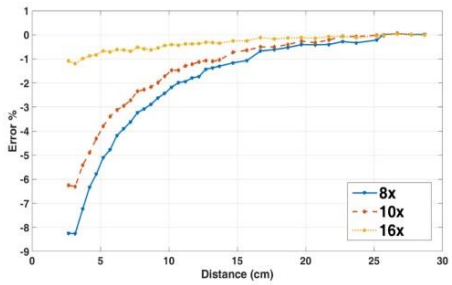

Figure 6: Reading error dependence on the number of the operating sensors, influence of the external DC current in superior position, Same weights method

V. CONCLUSION

Current through the busbar can be measured by array of the integrated fluxgate sensors, resolution of 1 mA is achievable. Placement of sensor array helps to significantly reduce the influence of the crosstalk fields. The maximum measured current for 16 sensors configuration is 400 A, but this range can be easily changed by increasing the distance from the sensor to the busbar. The main advantages of the new method compared to the industry standard are 10-times lower noise, 10-times better temperature stability, more compact size, same low crosstalk error and lower price. The disadvantages of our sensor are the need of DAQ card, digital processing of the output signals, and power consumption of the multi-sensor system. Now the current transducers are installed on the neutral line of a distribution transformer located in the Czech Republic for the long-term measurements the geomagnetically induced currents.

ACKNOWLEDGMENT

This work was supported by the Grant agency of the Czech Republic through the project "New methods for the measurement of electric currents" (GACR 17-19877S).

REFERENCES

[1] P. Ripka, Electric current sensors: a review, Meas. Science and Technology 21 (2010) Iss. 11, pp.1-23.

[2] Ajbl, A.; Pastre, M.; Kayal, M. A fully integrated Hall sensor microsystem for contactlessw current measurement. IEEE Sensors J. 2013, 13, 2271–2278, 10.1109/JSEN.2013.2251971

[3] DRV425 Fluxgate Magnetic-Field Sensor, Texas Instruments datasheet at http://www.ti.com/product/DRV425/datasheet

[4] P. Ripka, A. Chirtsov, Busbar current transducer with suppression of external fields and gradienrs, IEEE Transaction on Magnetics, Volume 54, Issue: 11, 2018

[5] A Busbar Current Sensor With Frequency Compensation Pavel Ripka, Václav Grim, and Vojtech Petrucha IEEE TRANSACTIONS ON MAGNETICS, VOL. 53, NO. 4, APRIL 2017

[6] P. Ripka, M. Pribil, V. Petrucha, V. Grim, K. Draxler, A Fluxgate current sensor with an Amphitheater Busbar, IEEE Transactions On Magnetics, Vol. 52, Issue 7, July 2016

[7] Z. Zhenhong, O. Syuji, A. Osamu, and K. Hideto, "Development of the highly precise magnetic current sensor module of +/−300 A utilizing AMR element with bias-magnet," IEEE Trans. Magn., vol. 51, no. 1, pp. 1–5, Jan. 2015.

[8] L. Di Rienzo, Z. Zhang, "Spatial harmonic expansion for use with magnetic sensor arrays", IEEE Trans. Magn., vol. 46, no. 1, pp. 53-58, Jan. 2010

[9] Weiss, R., Makuch, R., Itzke, A., & Weigel, R. Crosstalk in Circular Arrays of Magnetic Sensors for Current Measurement. IEEE Transactions on Industrial Electronics, 2017, 64.6, 4903-4909

[10] Mlejnek, P., Vopálenský, M., Ripka, P. AMR Current Measurement Device. Sensors and Actuators., 2008, 141(1-3), 646-653.

[11] M. Mirzaei, P. Ripka, A. Chirtsov, P. Kaspar, J. Vyhnanek , The effect of conductor permeability on electric current transducers, AIP Advance 8, 047506, 2018